Single bubble dynamics during nucleate flow boiling on a vertical heater: Experimental and theoretical analysis of the effect of surface wettability,roughness and bulk liquid velocity

Sarker, D.; Ding, W.; Schneider, C.; Hampel, U.;

Single bubble dynamics during nucleate flow boiling on a vertical heater: Experimental and theoretical analysis of the effect of surface wettability, roughness and bulk liquid velocity

D. Sarker[a], W. Ding[a,b], C. Schneider[c], U. Hampel[a,b]

[a] Helmholtz-Zentrum Dresden-Rossendorf (HZDR), Institute of Fluid Dynamics, Bautzner Landstraße 400, 01328 Dresden, Germany

[b] Technische Universität Dresden, Chair of Imaging Techniques in Energy and Process Engineering, 01062 Dresden, Germany

[c] University of Applied Sciences Zittau/Görlitz, Institute of Process Technology, Process Automation and Measuring Technology, 02763 Zittau, Germany

Abstract

The present study reports the mutual effect of heater surface wettability, roughness and bulk liquid velocity on the bubble dynamics and departure in nucleate boiling. Boiling experiments were conducted at atmospheric pressure with degassed-deionized water at low subcooling (1.9 ± 0.25 K) for vertically oriented stainless steel heaters. Self-assembled monolayer (SAM) coating and wet-etching technique were used to alter the heater surface wettability and roughness. Liquid contact angle hysteresis (θ_{hys}) and root mean square roughness (Sq) of the heater surfaces were adjusted between $42.32° \leq \theta_{hys} \leq 68.56°$ and roughness $0.01\,\mu\text{m} \leq Sq \leq 0.549\,\mu\text{m}$. High resolution optical shadowgraphy has been used to record the bubble life cycle. Experimental results show that higher bulk liquid velocity yields smaller bubble departure diameters for all heater surface characteristics. Bubble departure diameters are greater for low wetting surfaces. The bubble growth rate and departure diameter were found maximum for an intermediate surface roughness Sq between 0.108 and 0.218 μm. The corresponding roughness height is referred to as the 'optimal roughness height' in this study. Eventually, a bubble departure criterion was derived from the expressions of forces which act on a nucleating bubble throughout its growth cycle. 90% of the departing bubbles satisfy the bubble departure criterion with $\pm 25\%$ deviation.

Keywords: bubble growth, bubble departure, surface wettability, roughness, flow boiling.

Nomenclature

C_{eff}	constant, quantifying the effect of heater surface characteristics on bubble growth		ΔT_{sub}	subcooling temperature (K)
			ΔT_w	wall superheat (K)
c_p	specific heat capacity (J/kgK)		θ	liquid contact angle (°)
d_w	bubble base diameter (m)		ϕ	bubble inclination angle (°)
D	diameter (m)		ν	kinematic viscosity (m²/s)
f	bubble frequency (1/s)		ρ	density (kg/ m³)
F	force (N)			
g	gravitational acceleration (= 9.81 m/s²)		*Subscripts*	
G_s	non-dimensional liquid shear gradient			
h	heat transfer coefficient (W/m²K)		*adv*	advancing
h_{lv}	latent heat of evaporation (J/kg)		*b*	bubble
k, K	thermal conductivity (W/mK), area influential factor		*c*	condensation, conduction
			cm	center of mass
m	constant, fraction of the bubble height		*d*	departure
N_n	nucleation site density (1/m²)		*eff*	effective
Nu	Nusselt number		*eq*	equivalent
Pr	Prandtl number		*ev*	evaporation
q''	heat flux density (W/m²)		*fc*	forced convection
r	radius (m)		*g*	growth
Re	Reynolds number		*hys*	hysteresis
Sq	root mean square roughness of surface (μm)		*i*	interface
St	maximum roughness height of surface (μm)		*l*	liquid
t	time (s)		*ml*	microlayer
T	temperature (K)		*qc*	quenching
			rec	receding
Greek symbols			*v*	vapor
			w	heater wall, waiting period
α	advancing bubble contact angle (°)		*x*	normal to the heater wall
β	receding bubble contact angle (°)		*y*	upward direction
δ	thermal liquid layer thickness (m)			

1. Introduction

1.1 Motivation

Nucleate boiling is one of the most important modes of heat transfer. It which involves complex mass, momentum and energy transfers which take place at the interfaces (solid-gas, solid-liquid,

liquid-gas, gas-liquid-solid) and the bulk [1]. Different parameters, such as fluid properties, subcooling, bulk liquid velocity, system pressure etc. have effect on the bubble dynamics. Mass flux and system pressure are found as very influential to the bubble departure [2] and nano-micro patterned surfaces [3, 4] have significant role on the boiling heat transfer. Hence investigating the impact of heater surface characteristics and bulk liquid velocity on a single nucleated bubble is crucial for further scientific understanding and optimization of boiling heat transfer. The study reported in this paper was performed to investigate the mutual influence of heater surface wettability, roughness and bulk liquid velocity on the bubble dynamics and departure in nucleate boiling. The total evaporative, quenching and convective heat flux in nucleate boiling are:

$$q''_{ev} = \frac{\pi}{6} D_d^3 \rho_v h_{lv} f N_n. \qquad\qquad [5] \qquad\qquad\qquad (1\ a)$$

$$q''_{qc} = 2\sqrt{\frac{k_l \rho_l c_{p,l}}{\pi t}} \left(T_w - T_{sat}\right) t_w f K \frac{\pi D_d^2}{4} N_n. \qquad [6] \qquad\qquad\qquad (1\ b)$$

$$q''_{fc} = h_{fc} \left(\Delta T_w + \Delta T_{sub}\right) K \left(1 - \frac{\pi D_d^2}{4}\right) N_n. \qquad [7] \qquad\qquad\qquad (1\ c)$$

Here, K is a bubble influence factor which was suggested as $K = 0.5$ in a recent study [8]. Among the different parameters of the bubble ebullition cycle the bubble departure diameter (D_d) is one of the most important ones (Eqns. 1 a, b, c) as it is associated with latent heat. Eqn. 1 (a) shows that the total latent evaporative heat transfer (q''_{ev}) has a cubic dependency on the bubble departure diameter and thus a slight uncertainty of this parameter can notably deteriorate the accuracy of the total heat transfer calculation. The departing bubble also has a strong influence on the transient conduction heat transfer. Quenching heat transfer (q''_{qc}) due to the transient heat conduction was found to dominate the total heat transfer [7]. Usually, the contribution of the liquid phase convective heat transfer (q''_{fc}) to the total heat transfer is less [7]. Thus, it can be concluded that the departure dynamics of an isolated nucleated bubble is crucial for the estimation of the wall boiling heat transfer. Therefore, in the following, the basic physics of the bubble departure process will be explained.

1.2 Physical process of bubble departure

In simple words, the bubble departure criterion can be defined as a condition in which a growing bubble leaves the cavity and the cavity mouth is free for the growing of a subsequent bubble. Hence it can be defined by the condition $y_{cm} > r_w$ where the bubble inclination angle is assumed to be

69 related with the movement of apparent contact lines of the bubble base. High resolution optical

70 observations manifest that the bubble departure comprises of complex mechanisms. Jung and Kim

71 [9] observed the complete depletion of the microlayer beneath the nucleated steam bubble on a

72 horizontal surface during the growth period and then, that the bubble base shrank. The shrinkage of

73 the bubble base was followed by departure [10]. Pool boiling on a vertical surface is more

74 complicated than on a horizontal surface, because the bubbles grow at an angle with respect to the

75 heater surface in response to the upward buoyancy force. Therefore, forces acting on the bubbles are

76 directed normal and parallel to the heater wall. In this case, bubbles may depart from the nucleation

77 site by sliding, which is not the case for pool boiling on a horizontal heater [11]. The departure of a

78 steam bubble is appreciably more complex in flow boiling conditions.

79

80 The bubble departure criterion is often derived using force balances [2, 12]. Table 2 summarizes the

81 equations of different forces and Fig. 2 shows their directions. The forces, such as buoyancy (F_b),

82 unsteady drag (F_{du}), quasi-steady drag (F_{qs}), surface tension (F_s), additional-added mass

83 ($F_{growth, bulk}$), shear lift (F_{sl}), contact pressure (F_{cp}) and hydrodynamic pressure (F_h) force were well

84 explained by several investigators [2, 11-14]. When the sum of the forces along the flow direction is

85 just greater than zero, then the bubble departs. Klausner et al. [13] compared F_{sx} and F_{qs} for flow

86 boiling conditions and argued that F_{sx} is not sufficient to prevent a vapour bubble from departure.

87 Due to the asymmetrical bubble growth on the heater surface, liquid drag on the bubble surface

88 exhibits an unsteady drag force (F_{du}). This force may act opposite to the flow direction and is

89 important in holding the bubble at its nucleation site prior to departure. Thorncroft et al. [11]

90 introduced an additional-added mass force ($F_{growth,bulk}$) which is associated with the bubble growth

91 for flow boiling, acts entirely in the positive y-direction and assists the bubble departure. The bubble-

92 liquid interface experiences a quasi-steady drag force (F_{qs}) due to the bubble velocity (V_b) relative to

93 the bulk liquid velocity (V_l) that acts parallel to the flow direction. F_{qs} was suggested as the

94 dominant force for the bubble departure condition on a horizontal heater surface by Klausner et al.

95 [13]. Chang [15] combined the static forces (F_b, F_s) with the dynamic forces (F_{qs}, F_{sl}) to develop a

96 bubble departure criterion for flow boiling on an inclined surface. The significant forces for the

97 bubble departure on vertical heaters in Cho et al. [16] were supposed to be F_b, F_s, F_{du} and F_{qs}.

98 Sugrue and Buongiorno [5] performed a sensitivity analysis to find out the dominant forces for

99 different mass fluxes. The bubble departure mechanism was found to be sliding for low mass flux

100 where F_b and F_{sy} are dominant. For a high mass flux regime, F_{sx} and F_{sl} were found more influential

101 for the bubble detachment.

1.3 Effect of heater surface characteristics and bulk liquid velocity on bubble departure

103

104 The impact of heater surface characteristics on the bubble dynamics may be understood through the
105 thermo-hydrodynamics of the microlayer beneath a nucleated bubble. Numerous groups employed
106 the shadowgraph imaging technique to investigate the effect of heater surface wettability [17-21] and
107 roughness [22-24] on the bubble dynamics and departure for pool and flow boiling. Phan et al. [17]
108 found larger bubbles and lower bubble emission frequencies for the well-wetting surfaces. Bubble
109 departure diameters were found almost 3 times larger on the hydrophobic surface [18] and 2 times
110 smaller on the hydrophilic surface [19] compared to the uncoated silicon surface for horizontal pool
111 boiling. Rousselet [20] studied the effect of heater surface wettability on the bubble departure
112 diameter for a wide range of bulk liquid velocities (0 - 0.30 m/s) but his findings were inconclusive.
113 Bubble sliding velocities were found greater [22] and the sliding distances were shorter for well-
114 wetting surfaces [20, 22]. Bubble base diameters were found to increase for the surfaces with larger
115 liquid contact angle [22]. Jo et al. [25] claimed that the direction of the surface tension at the triple-
116 point (three-phase intersection) is towards the generated bubble side for the hydrophilic cases and
117 outward of the vapor bubbles for the hydrophobic cases. Therefore, a hydrophobic heater surface
118 results in a larger contact area than a hydrophilic surface. Consequently, larger bubbles are generated
119 on the hydrophobic surfaces. Roughness, though being one of the main parameters of surface
120 characteristics, has been so far a lesser subject of investigations according to the available literature.
121 However, it can be hypothesized that even small-scale increase of surface roughness may increase
122 the evaporative heat transfer area, as the ratio of actual to projected surface area is higher for rough
123 surfaces. Kruse et al. [26] fabricated surface structures via a femtosecond laser surface processing
124 technique. The influence of surface roughness (Rq = 1.4-7.8 µm) on the heat transfer coefficients at
125 lower heat flux were not conclusive in their study. Goel et al. [23] studied the effects of stainless
126 steel surface roughness (Ra = 0.50-3.54 µm) on the bubble departure for subcooled nucleate pool
127 boiling. They found that the departure diameter decreases as the surface roughness increases. They
128 did not addressed the interactions of the heater surface profile and the microlayer dynamics, though
129 they are important [27]. Kim et al. [4] observed a larger bubble size and a lower bubble frequency on
130 the designed surface structure due to the trapped superheated liquid layer between the
131 microstructures. Zou et al. [3] reported an early evaporation of microlayer beneath the bubble base.
132 An almost 5.25 times higher bubble growth rate was found on the ridge-structured surface compared
133 to a plain surface. Sarker et al. [22, 27] found that the heat transfer to the bubble was the greatest due
134 to the maximum microlayer evaporation rate at an intermediate roughness height.

135　The bulk liquid velocity is another important parameter that impacts the bubble dynamics. Several

136　studies asserted that for higher bulk liquid velocity the bubble growth rate and the departure diameter

137　decrease [2, 20, 28]. The bubble growth rate significantly influences the departure diameter and they

138　are positively correlated [20]. One of the reasons for decreasing the bubble growth rate could be that

139　the increase of bulk liquid velocity leads to a decrease in thermal boundary layer thickness on the

140　heater surface which decreases the heat diffusion to the bubble [20]. Yoo et al. [29] performed

141　experiments for HFE-301 on vertical ITO film heaters for upward subcooled flow boiling conditions.

142　Their findings are in agreement with other groups [2, 30]. That is, bubble size and axial bubble

143　velocity decreased and the bubble release frequency increased with the increase of bulk liquid

144　velocity. Condensation heat transfer on the bubble surface due to the bulk liquid velocity also affects

145　the bubble departure diameter. Condensation rate increases with the bulk liquid velocities, thus

146　bubble growth rate and bubble departure diameter may decrease.

147

148　The literature survey concludes that heater surface wettability, roughness and bulk liquid velocity

149　have significant impact on the bubble departure. However, mutual influence of these parameters on

150　the bubble dynamics was not investigated in the above-mentioned studies. Moreover, existing bubble

151　departure models do not account the role of heater surface characteristics. Currently the force

152　balance approach is extensively used to define a bubble departure criterion, though the expressions

153　for different forces consist of empirical constants. Therefore, experiments have been performed in

154　this work to take into account the simultaneous impact of these parameters (surface wettability,

155　roughness and bulk liquid velocity) on the bubble departure for vertically oriented heaters. The

156　article is structured as follows. Section 2 delineates the surface preparation techniques for the

157　examined heater surfaces, the experimental setup, measurement techniques, experimental procedure

158　and relevant uncertainties. Section 3 discusses the experimental findings for the role of surface

159　characteristics and bulk liquid velocity on the bubble dynamics and departure. We have formulated a

160　simpler expression for the bubble departure criterion in section 4. Section 5 eventually summarizes

161　the results and gives a general outlook.

162

163　**2.　Experiment**

164

165　In order to stay close to the practice, 0.5 mm thick stainless steel heater plates were used in the

166　experiments, as steel is common in many heat transfer applications. The thermal conductivity and the

167　electrical resistivity of the used stainless steel material were 15 W/mK and 0.73 Ω mm²/m at 20°C,

168　respectively. The deposition of chemicals on surfaces also modifies the surface wettability. Self-

assembled monolayer (SAM) coating, chemical vapor deposition (CVD) or oxidation technique can change the surface wettability without altering the roughness noticeably. Deposition of ultrathin layers is one of the reliable methods for influencing the surface wettability and investigating the isolated bubble dynamics in nucleate boiling. In total, 9 different test surfaces were treated by various techniques in order to get a range of surface wettability and roughness in the present study. The surface preparation methods, which were used are wet-etching and self-assembled monolayer (SAM) coating. A surface roughness height (St) of less than ~5 µm is suitable for investigating isolated bubbles in nucleate boiling. This limit of surface profile height was found during experiments in this work for a wide roughness range. A surface profile height with more than 5 µm may act like bubble nucleation cavities. Geometry and shape of a cavity were kept constant, to nullify their effect on the bubble dynamics. The surface preparation and analyzing techniques are explained below.

2.1 Surface preparation and analyzing

All the test surfaces were mirror polished with root mean square roughness $Sq \leq 0.01$ µm prior to employment of other surface treatment techniques. Wet-etching was used to control the roughness of surfaces. 6 stainless steel surfaces were etched by dipping polished samples in an acid solution (H_2O: HCL: $HNO_3 = 6:6:1$) for a time period in the range of 5 to 35 mins at room temperature. Generally, surfaces get rougher when dipping periods are longer. The acidic solution of wet-etching method removes a layer of material from the surfaces. Therefore, the roughness of a wet-etched surface does not solely depend on the etching period and the chemical composition of the solution, but also on the elemental composition, grain size and orientation of the solid material. The self-assembled monolayer (SAM) coating was used to modify the wettability of 4 stainless steel surfaces. Among 4 of these samples, 2 were mirror-polished and other 2 were wet-etched. SAM is done by depositing a layer of molecules on a substrate by simply dipping it in a special liquid solution. According to literature, the monolayer is ultra-thin and the length of a formed C-C single bond is about 0.15 nm. An SAM layer is about 10 carbon atoms, which is around 1-1.5 nm thick. As the thickness of SAM coating is in the nanometer scale, it does not influence the roughness of surfaces notably. The SAM coating method explained in Harm et al. [31] was applied in this study to modify the wettability of surfaces. Polished and rough surfaces were coated by Heptadecafluorodecylphosphonic acid (HDPA) (CAS 80220-63-9) and Etidronic acid (EDA) (CAS 7414-83-7) to decrease and increase the surface wettability, respectively.

The surface wettability was assessed using a goniometer (DataPhysics OCA 30) following the dynamic liquid contact angle measurement method rather than the static liquid contact angle. Dynamic liquid contact angles were measured following the sessile drop method. Thus, both the advancing θ_{adv} and receding θ_{rec} liquid contact angles of the treated surfaces were captured. The liquid contact angle hysteresis is calculated as $\theta_{adv} - \theta_{rec} = \theta_{hys}$. The liquid contact angle hysteresis is the results of the pinning effect of the three-phase contact line. The significance of liquid contact angle hysteresis to characterize a surface has been extensively investigated by different groups and they concluded that it arises from the surface roughness and/or heterogeneity [32]. A non-contact optical method namely confocal microscopy (µsurf expert, xy-resolution: 0.3-3µm, z-resolution: 3 nm) was used to analyze the surface topography. The images of surface topography were obtained with a 50x lens over an area of 320 µm x 320 µm. From these images, the 2D and 3D profiles were created and the roughness parameters (Sa, Sq, St etc.) were calculated in accordance with the international standard ISO 25178. The measurement errors arising from noise and slight vibrations of the surroundings were reduced during analysis by setting the z thresholds carefully. The details of surface preparation techniques and the corresponding surface wettability and topology information are shown in Fig. 2.

Two polished surfaces were coated with the HDPA and EDA and yielded θ_{hys} = 65.30° and θ_{hys} = 42.32°. The liquid contact angle hysteresis of the uncoated polished surface was 49.22°. Thus, we obtained 3 different wetting surfaces where roughness effect on the boiling is negligible. We found that the surface roughness increased with the etching duration (Fig. 2). The minimum etching period was 5 mins and the maximum one was 35 mins which produce a Sq of 0.108 µm and 0.549 µm. Monolayer coatings were also deposited on two rough surfaces (Sq = 0.266 µm and 0.392 µm) to change the wetting characteristics of them. The HDPA and EDA coatings on the surfaces with Sq = 0.266 µm and Sq = 0.392 µm gave a liquid contact angle hysteresis of θ_{hys} = 68.55° and θ_{hys} = 45.95°, respectively. Test surfaces had different roughness (Sq = 0.108, 0.218, 0.406 and 0.549 µm) which θ_{hys} is 59.97°±1.50°. However, this study addresses the role of heater surface roughness (Sq in the range from ~0.01 to 0.549 µm) and surface wetting characteristics on the bubble dynamics. The surface wettability and roughness has been measured at 6 different locations on the surfaces for each kind of preparation. The surface roughness and wettability were measured before and after the boiling experiments. The averaged values of these two measurements of the samples are used to characterize the surfaces. With the increase of surface roughness height deviations of surface profile measurement are increased. The deviations of Sq and St for polished surfaces were determined as

235 ± 0.00195 µm and ± 0.036 µm and for rough surfaces, they were ± 0.0275 µm and ± 0.285 µm,

236 respectively. The measurement of liquid contact angle also gives some uncertainty. The maximum

237 deviations for advancing liquid contact angle and liquid contact angle hysteresis were found to be

238 ± 2.952° and ± 4.109°. Test samples were cleaned before measuring the surface parameters (liquid

239 contact angle and surface roughness) and using them in the boiling experiments. Surfaces were

240 cleaned in an ultrasonic bath with ethanol at 40°C for 30 minutes. Liquid ethanol on the test surfaces

241 was dried by a nitrogen flow just after taking out the samples from the ultrasonic bath. To initiate

242 nucleate boiling in a well-defined position, a cylindrical artificial cavity of approximately 1963.5

243 µm² and 50 µm depth was prepared by the microlaser. The deviations in the preparation of the cavity

244 diameter were determined as ± 8.00%. The total size of the heater which was used in the boiling

245 experiments was 130 x 20 mm².

246

247 *2.2 Flow boiling experiments and measurement techniques*

248

249 A subcooled flow boiling loop was used for investigating the isolated bubble dynamics in upward

250 flow boiling experiments. The experiment was conducted at 1 atmospheric pressure using deionized

251 water. A schematic diagram of the flow boiling loop is shown in Fig. 3. The test facility was

252 constructed earlier for a nucleate boiling experiment [33]. For the present study, the test section and

253 the flow meter with its connections of the loop were modified. The main components of the flow

254 loop were a pump, a preheater, a flow meter, a degasser, a filter, an air-cooled condenser and a test

255 section (see Fig. 3). A special pump with low net positive suction head (NPSH) of lower than 0.5 m

256 at 6 m³/h was used to circulate the test fluid. An electric preheater of 10 kW was installed

257 downstream of the pump and before the flow meter with a bypass valve to control the liquid

258 subcooling at the inlet of the test section. The electric power of the preheater was sufficient to

259 maintain the inlet liquid temperature close to the saturation temperature. The mass flow rate was

260 measured using a Krohne Optimass 1400 C Coriolis mass flow meter. The maximum range of the

261 flow meter was 1.806 kg/s with an accuracy of better than ± 0.20% of the actual measured value.

262

263 Fig. 4 shows the details of the test section. The test section comprises a 28 mm x 28 mm x 350 mm

264 rectangular flow channel. Three sides of the test section were made of borosilicate glass for optical

265 access to the heating surface. The rear panel of the test section consists of a stainless steel frame, a

266 block of thermal insulating polyether ether ketone (PEEK) which fixes the test heaters, the copper

267 connections for heating the heaters by the electric power and the treated stainless steel heaters

268 themselves. The thermal conductivity and the specific volume resistivity of the PEEK are 0.25

269 W/m.K and 10^{16} ohm-cm, respectively. Before fixing the PEEK block with the test heaters in the

270 stainless steel frame, temperature resistant silicon paste (thermal conductivity 0.18 W/m.K) was used

271 to glue the gaps between the test samples and the PEEK block. The back panel of the test section was

272 fixed and sealed properly with the borosilicate glass parts. A narrow channel was fabricated in the

273 PEEK block and a K-type thermocouple was inserted through the narrow channel which touched the

274 back side of the test heater surfaces for measuring the heater wall temperature.

275

276 The loop was flashed and rinsed with deionized water and acetone before performing the

277 experiments. At that time, the water which flows through the loop was filtered as well to remove

278 impurities if there were any. The loop was then filled up with deionized water. The entrapped gases

279 in the different components of the loop were released with the help of valves and the loop was

280 completely filled up with water. Then the boiler was turned on for degassing the liquid. The

281 deionized water in the boiler was heated up to saturation temperature for more than 2 hours without

282 fluid flow. For further degassing, the water was pumped through the loop at low flow velocity and

283 low subcooling. The pump and the preheater were keep running for some time, so that the dissolved

284 gases would be removed completely. This process took around 1 hour. When the liquid was

285 sufficiently degassed, the power source was switched on to generate bubbles from the artificial

286 cavity. The test heaters were operated for some time to get rid of entrapped gases in the cavities of

287 the surfaces. The heating power was in the range of 39.41 kW/m² - 45.47 kW/m². The desired bulk

288 liquid velocities were obtained by adjusting the bypass valves and the rotational speed of the pump,

289 which were measured by the flow meter. It is worth mentioning that special care was taken to keep

290 the stainless steel heater surfaces clean. Once the bulk liquid velocity and the bubble ebullition cycle

291 were in steady state, the data was collected. The temperatures of the liquid at the inlet and outlet of

292 the test section were measured by the calibrated K-type thermocouples. The liquid subcooling at the

293 inlet of the test section was set to 1.9 ± 0.25 K with the help of the preheater. For each test run, the

294 bulk liquid velocity and the heating power were adjusted. Thus the heating power and the flow rate

295 were acquired. Also, the inlet and outlet temperatures of the test section and the heater wall

296 temperature were measured.

297

298 High resolution optical shadowgraphy using a MotionPro high-speed video camera

299 (1280 x 1024 pixels and 1030 frames per second) equipped with an AF Micro-Nikkor 105 mm

300 f/2:8D lens was employed for recording the bubble life cycle. A wide-open aperture (f/2.8) provides

301 a shallower depth of field and the bubbles were focused and captured in this mode. This way, sharp

302 bubble images were obtained while all background structures have been blurred out. The recording

303   speed of the camera was 2,500 frames per second while the spatial resolution was 16.40 ± 1.50 μm

304   per pixel. The stacks of images from the high-speed video camera were processed using the image

305   processing software ImageJ. The major steps of image processing are explained in other articles [22,

306   24]. The bubble base diameters were estimated in this study as well. For that, the temporal evolutions

307   of the vapor bubble-solid interfaces were captured using a tool of the ImageJ called 'Orthogonal

308   views'. A simple Matlab script was written to evaluate the bubble departure diameters in terms of the

309   bubble base radius and the center of mass of a bubble in the upward direction.

310

311   *2.3 Uncertainty analysis*

312

313   Optical shadowgraphy has several sources of uncertainty. Apart from the static uncertainty of the

314   camera sensor, the imaging technique has got a spatial uncertainty which was estimated from the

315   pixel resolution. Another source of uncertainty is the geometry analysis of the bubbles. Altogether,

316   the uncertainty of imaging is ± 0.0409 mm. The thermocouples were calibrated against a reference

317   thermometer with a temperature range from 40°C to 120°C. The deviation of the reference and the

318   measured values of thermocouples increased with temperature. The maximum deviation of a

319   thermocouple was estimated as ± 0.3 K when calibrated for temperatures above 90°C. As mentioned

320   above, the thermocouples were used to measure the heater wall temperature and the liquid

321   temperature at the inlet and outlet of the test section. The fluctuations in temperature reading for each

322   test run were noticed and all these data points were averaged. Thus, the total uncertainties of the

323   liquid temperature at the inlet and outlet of the test section were ± 0.58 K and ± 0.54 K, respectively.

324   Only one thermocouple was used to measure the heater wall temperature. Hence, it can be seen as an

325   area- and time-averaged wall temperature. The measured wall temperature for low flow velocity was

326   compared against the correlations for wall temperature calculation [34, 35] and a deviation of

327   ± 0.63 K was found. Due to the uncertainty in single measurement the total uncertainty for the wall

328   temperature measurement is ± 0.70 K. The uncertainty of the flow rate measurement is $\pm 1.70\%$.

329   This uncertainty may arise from small fluctuations of the fluid flow caused by the different

330   components of the loop and particularly the flow meter. In the heat flux measurement of the test

331   heaters, heat losses cause uncertainty. The possible sources of uncertainties in the heat flux (q'')

332   calculation are the power supply ($\pm 0.50\%$), the fluctuations in measuring the power ($\pm 1.55\%$), the

333   extended heater surface area ($\pm 4.80\%$), the long connecting cables and connections ($\pm 5\%$). The heat

334   loss occurs due to the dissipation of heat to the environment through the insulating materials (3%).

335   All these uncertainties were considered in the heat flux calculation and are given in Table 1.

336   Parameters, such as bubble diameter, bubble base diameter and center of mass position we ensemble-

337 averaged for many single bubbles (typically 25). According to the so-called three-sigma rule, 68.27%

338 of the captured curves of the bubble ebullition cycles were one standard deviation away from the

339 averaged values and one standard deviation was ± 0.0458 mm. For the sake of clarity, the following

340 graphs just represent the exemplary curves.

341

342 **3. Results and discussions**

343

344 In this section, the typical bubble life cycles for different bulk liquid velocities (0.052 m/s and

345 0.183 m/s) which are captured by the high speed video camera are shown (sub-section 3.1). This

346 section also describes the detailed experimental results of the study on the mutual effect of heater

347 surface wettability, roughness and bulk liquid velocity on the bubble dynamics (sub-section 3.2) and

348 bubble departure (sub-section 3.3) for nucleate boiling.

349

350 *3.1 Typical bubble life cycle*

351

352 Figs. 5 (a, b) shows the snapshots of the bubble ebullition cycles, captured by a high-speed video

353 camera for 2 different liquid velocity (0.052 m/s, 0.183 m/s) on a low-wetting polished surface

354 ($Sq = 0.01$ μm, $\theta_{hys} = 65.3°$). Our imaging technique had sufficient resolution to record the each

355 major stage of a bubble life cycle. It includes bubble generation (i), growth (ii), departure (iii),

356 sliding (iv), lift-off or detachment (v) and the consecutive bubble generation from the same cavity

357 (vi). The corresponding time period for each steps are showed in milliseconds on the images of

358 Figs. 5 (a, b). We see that the bubble diameter and the departure period decrease with the increase of

359 the bulk liquid velocity. On the other hand, the bubble waiting period is much longer for the higher

360 bulk liquid velocity.

361

362 *3.2 Effect of heater surface characteristics and bulk liquid velocity on the bubble dynamics*

363

364 This sub-section reports the mutual effect of heater surface characteristics and bulk liquid velocity on

365 the temporal evolution of the bubble equivalent diameter (D_{eq}), bubble base diameter (d_w) and center

366 of mass in y-direction (y_{cm}). The results are presented for a range of bulk liquid velocity (0.052 –

367 0.183 m/s (approx.)) with three different heater surface characteristics ($Sq = 0.01$ μm, $\theta_{hys} = 65.30°$;

368 $Sq = 0.218$ μm, $\theta_{hys} = 61.47°$ and $Sq = 0.549$ μm, $\theta_{hys} = 58.47°$) and heat flux (39.41 - 45.47

369 kW/m²) in Figs. 6-8. The general findings are that bubble equivalent diameters and departing bubble

370 diameters are larger for lower bulk liquid velocity (Figs. 6 a, 7 a and 8 a). Not only the bubble

371 equivalent diameter but also the bubble growth rate is faster for lower bulk liquid velocity. Higher

372 bulk liquid velocity reduces the bubble base diameter for a low-wetting smooth surface (Fig. 6 b). A

373 contraction effect at the bubble bases is noticed at the moment of bubble departure for this surface

374 ($\theta_{hys} = 65.30°$) when the bulk liquid velocities are between 0.052 m/s and 0.183 m/s. If the bulk

375 liquid velocity is increased more (0.255 m/s), the bubble base expands during departure (Fig. 6 b)

376 and the bubble moves a comparatively smaller distance along the flow direction prior to

377 departure (Fig. 6 c). Fig. 7 b shows that the bubble base diameter is found to be negatively correlated

378 with the bulk liquid velocity (0.052- 0.12 m/s) for a rough surface ($Sq = 0.218$ μm, $\theta_{hys} = 61.47°$).

379 The expansion rates of bubble base diameters for another rough surface ($Sq = 0.549$ μm,

380 $\theta_{hys} = 58.47°$) are almost equal until 2 ms of their growth period at different bulk liquid velocities

381 (Fig. 8 b). After 2 ms, the bubble base experiences contraction and expansion effects. Hence this

382 surface ($Sq = 0.549$ μm, $\theta_{hys} = 58.47°$) does not show distinguishable correlations between the bulk

383 liquid velocity and the bubble base diameter (Fig. 8 b).

384

385 The bulk liquid velocities are found to be positively correlated with the moving distance of center of

386 mass prior to departure for the surface with $Sq = 0.218$ μm (Fig. 7 c). Fig. 7 (c) further shows that

387 until 5 ms of the bubble growth, the bubble movement in the upward direction is faster for higher

388 bulk liquid velocity. The center of mass of bubbles (Fig. 7 c) for the rough surface ($Sq = 0.549$ μm,

389 $\theta_{hys} = 58.47°$) does not show a correlation with the bulk liquid velocities. Bubble departure periods

390 are found inversely correlated with the bulk liquid velocity for $Sq = 0.01$ μm and 0.218 μm. For

391 $Sq = 0.549$ μm, though the difference between the bubble departure periods for a range of bulk liquid

392 velocity (0.052 m/s-0.183 m/s) is comparatively small (4 ms-5.6 ms), still the bubble departure

393 period is positively correlated with the bulk liquid velocity (Fig. 8 c).

394

395 The bubble growth rate, from the view of the heat transfer, has been discussed here. Different heat

396 transfer processes, namely the microlayer evaporation, the heat diffusion through the bubble surface

397 and the condensation heat transfer contribute in the growth of a bubble. A previous article [27] of our

398 group showed that the heater surface characteristics has non-linear relationship with the microlayer

399 evaporation and the bubble growth. It was found that the bubble growth rate is the maximum for an

400 intermediate roughness. This section also shows that the bubble growth rate is maximum for

401 $Sq = 0.218$ μm compare to $Sq = 0.01$ μm and 0.549 μm. Figs. 6 a, 7 a and 8 a show that the bulk

402 liquid velocity impacts the bubble growth rate even in the initial growth period (< 2 ms).

403   Jung and Kim [36] found that the velocity of the microlayer boundary increases with the bubble

404   growth rate. Hence, the bulk liquid velocity may also have influence on the microlayer evaporation.

405   It implies that the microlayer area is positively correlated with the bubble growth rate and negatively

406   correlated with the bulk liquid velocity. The contribution of the heat diffusion through the bubble

407   surfaces reduce with the increase of the bulk liquid velocity, because $Re \propto Nu \propto 1/\delta_w$. On the other

408   hand, the heat transfer coefficient of condensation is greater for the higher liquid velocity as

409     $Nu_c \propto h_c$.

410

411   *3.3 Effect of heater surface characteristics and bulk liquid velocity on the bubble departure*

412

413   It was already indicated in the previous sub-section that the bubble departure diameter decreases with

414   the increase of bulk liquid velocity. Sugrue et al. [2] and Rousselet [20] also found similar influence

415   of bulk liquid velocity on the bubble departure diameter. Bubble departure diameters for different

416   heater surfaces are plotted with respect to the bulk liquid velocity for the heat flux range of 42.44 ~

417   45.47 kW/m² in Fig. 9. The dash-dot thick trend line represents the average of measured bubble

418   departure diameters for each surface. It shows that in spite of the effect of heater surface

419   characteristics, the bubble departure diameter decreases while the bulk liquid velocity increases. The

420   impact of liquid velocity on the bubble departure diameters is less at high bulk liquid velocity

421   (0.183 - 0.255 m/s). Bubble diameters are more scattered at a bulk liquid velocity from 0.052 to

422   0.105 m/s compared to a velocity from 0.105 to 0.255 m/s as depicted in Fig. 9. It proves that the

423   significance of the heater surface characteristics for the bubble departure diameter reduces with the

424   increase of the bulk liquid velocity.

425

426   Fig. 10 shows the effect of heater surface wettability on the bubble departure diameter (D_d). In

427   general, the bubble departure diameter has been found to increase with the liquid contact angle

428   hysteresis (θ_{hys}) from 42.32° to 65.30° for a range of bulk liquid velocities and heat fluxes. Bubble

429   departure diameters for a heat flux from 39.41 to 45.47 kW/m² and bulk liquid velocity from 0.052 to

430   0.183 m/s of a particular liquid contact angle hysteresis were averaged. A trend line of the averaged

431   bubble departure diameters is shown in Fig. 10. It shows that the averaged bubble departure diameter

432   increases from 0.75 to 1.70 mm while the liquid contact angle hysteresis increases from 42.32° to

433   65.30°. A closer look on Fig. 10 shows that the slope of the trend line is stronger for θ_{hys} between

434   49.22° and 65.30° than that from 49.22° to 42.32°. One of the main reasons for an increase of D_d

435 with θ_{hys} is that the forces which hinder the bubble departure are greater for low-wetting surfaces

436 [18].

437

438 Fig. 11 includes the bubble departure diameters for a heat flux of 39.41 to 45.47 kW/m² and bulk

439 liquid velocity of 0.052 to 0.183 m/s. All these bubble departure diameters are shown by symbols

440 and are averaged here with respect to the root mean square roughness of the surface (Sq). A B-spline

441 curve is provided as a trend line (dash-dot thick line). The line shows that the bubble departure

442 diameter increases from the polished surfaces to the surfaces with $Sq = 0.218$ μm. Then it decreases

443 with the increase of surface roughness until $Sq = 0.549$ μm. Bubble departure diameters are found

444 greater for intermediate surface roughness (approximately, $Sq = 0.108 - 0.218$ μm). It should also be

445 underlined here that the impact of heater surface characteristics on the bubble departure dynamics

446 can be both impeding and promoting at different bulk liquid velocities. Next section analyzes these

447 phenomena.

448

449 **4. Theoretical analysis of bubble departure**

450

451 *4.1 Analysis of important parameters*

452

453 While a nucleated bubble grows on a vertical heater surface, several forces at the liquid-vapor and

454 vapor-solid interfaces come into play. The literature review in section 1 summarizes that buoyancy

455 (F_b), surface tension (F_s), unsteady drag (F_{du}), quasi-steady drag (F_{qs}) and additional added-mass

456 force ($F_{growth,bulk}$) are the dominant forces for the bubble departure. The expressions of the forces

457 consist of basic parameters, such as physical properties of the fluid ($\rho_l, \rho_g, \sigma, v$), slip velocity of the

458 bubble ($\Delta V = V_l - V_b$) and geometrical parameters of the bubble ($d_w, R, \alpha, \beta, \varphi$).

459

460 Table 2 recapitulates these forces and parameters. The bubble inclination φ angle is included in the

461 equation for unsteady forces. Though the contact angles (α, β) are expected to vary with the

462 expansion and contraction of the bubble base, some groups considered the bubble contact angles as

463 constant ($\alpha = 45°, \beta = 36°$ [13]). Measuring the time dependent bubble contact angle is complicated,

464 especially at flow boiling conditions. Therefore, the influence of bulk liquid velocity on the bubble

465 contact angles (α, β) is not fully conclusive until now. The present experiments were performed at

466 atmospheric pressure and low subcooling. Hence, the experimental boundary conditions do not alter

467   the fluid properties much. Thus, it can be assumed that the total sum of the forces changes with the

468   temporal evolution of geometrical parameters of bubbles.

469

470   The experimental results show that the bubble departure diameter is greater for a larger bubble base

471   diameter (d_w). Further, d_w is an important parameter in calculating F_s, F_{cp} and F_h. Among them, F_s is

472   recommended by many groups as a significant force that holds the bubble on the surface. Moreover,

473   F_b is greater for larger bubbles, as $F_b \propto R^3$. On that account, these two geometric parameters (R, d_w)

474   of a bubble play an opposite role in the bubble departure process. According to Klausner et al. [13],

475   unsteady drag force (F_{du}) acts towards the heater surface and Thorncroft et al. [11] suggested that

476   additional added mass force ($F_{growth,bulk}$) solely acts upward and expedites the bubble departure

477   process. The directions of these forces (F_{du}, $F_{growth,bulk}$) were already introduced in Fig. 2. The

478   bubble radius (R) and the bubble growth rate ($\dot{R}$), which are geometric parameters, are both factors of

479   F_{du} and $F_{growth,bulk}$. $F_{growth,bulk}$ is dependent on bulk liquid velocity (V_l) and F_{qs} is affected by relative

480   velocity ($\Delta V = V_l\text{-}V_b$). As a result, the bubble departure can be predicted by the bubble radius (R),

481   bubble base diameter (d_w), bubble growth rate ($\dot{R}$ or dR/dt) and relative velocity ($\Delta V=V_l\text{-}V_b$). F_b and

482    $F_{growth,bulk}$ increase largely over time for a growing bubble and they contribute a huge amount to

483   overcome the hindering exerted on a bubble by F_s, F_{duy} and F_{qs} during departure. F_b, $F_{growth,bulk}$ and

484   F_{duy} are third and second degree functions of bubble radius. It implies that the bubble size (R) and

485   bubble growth rate (dR/dt) play a significant role for bubble departure. The bubble departure for

486   different of heater surface wetting characteristics and roughness is analyzed below based on bubble

487   size (D_{eq}), base diameter (d_w), bubble growth rate (dR/dt) and relative velocity ($V_l\text{-}V_b$)

488   (Figs. 12 and 13).

489

490   Fig. 12 shows that bubble size (D_{eq}), bubble base diameter (d_w) and bubble growth rate (dR/dt)

491   increase with the liquid contact angle hysteresis. The effect of surface wettability on the relative

492   velocity before bubble departure and on the bubble growth rate seems opposite to each other.

493   However, surface tension force (F_s) and unsteady drag force (F_{duy}) on a bubble can be greater for

494   low-wetting surfaces, since D_{eq}, d_w and dR/dt are greater for a surface with higher liquid contact

495   angle hysteresis. Both of these forces retard the bubble departure. A large bubble size for a low-

496   wetting surface also leads to a greater buoyancy force (F_b). Additional-added mass force ($F_{growth,bulk}$)

497   and quasi-steady drag force (F_{qs}) may become greater with the decrease of surface wettability and

498   expedite the bubble departure process. Fig. 12 manifests that the bubble departure is comparatively

499   earlier and a bubble departure diameter is smaller for well-wetting surfaces. It means that the

500   geometrical parameters are comparatively less effective for low-wetting surfaces compared to well-

501   wetting surfaces in the bubble departure

502

503   The influence of surface roughness on the dominant parameters of bubble departure is shown in

504   Fig. 13. Bubble size (D_{eq}) and bubble base diameter (d_w) are larger for the intermediate roughness of

505    $Sq = 0.218$ μm. A relative velocity ($\Delta V = V_l\text{-}V_b$) is generally lower for $Sq = 0.108$ μm and it exceeds

506   0.12 m/s during departure. A common tendency of the temporal evolutions of bubble growth rate

507   (dR/dt) is that they become almost asymptotic at bubble departure. The bubble growth rate is lower

508   for $Sq = 0.549$ μm compared to the other two rough surfaces. The bubble departure diameter is

509   slightly smaller for $Sq = 0.108$ μm than for $Sq = 0.218$ μm, though the departure period is much

510   smaller for the former surface ($Sq = 0.108$ μm) compared to the latter ($Sq = 0.218$ μm).

511

512   Fig. 13 shows that the bubble departure periods are longer for larger bubble bases. Similar results can

513   be found in Fig. 12. Since the effect of bubble growth rate is indistinguishable for $Sq = 0.108$ μm and

514   0.218 μm, (Fig. 13), buoyancy (F_b) and additional added mass force ($F_{growth,bulk}$) must be

515   convincingly greater for surfaces with $Sq = 0.108$ μm. Surface tension force (F_s) towards the heater

516   wall is expected to be lower for $Sq = 0.108$ μm and greater for $Sq = 0.218$ μm due to the smaller and

517   larger bubble base diameter, respectively. The unsteady drag force (F_{du}) may be higher due to the

518   larger bubble size at $Sq = 0.218$ μm. The low-wetting surface ($\theta_{hys} = 65.30°$) in Fig. 12 and the

519   surface with the roughness of $Sq = 0.218$ μm in Fig. 13 were found to produce a larger bubble

520   departure diameter and a longer departure period. Thus, the behaviour of these two surfaces is

521   similar with respect to bubble departure size and period.

522

523   The non-zero d_w at bubble departure leads to the conclusion, that surface tension force (F_s) keeps

524   acting during departure. At such a condition, a bubble departs from the cavity, slides, but does not

525   detach from the surface. Hence, the departure mechanism for the bubbles in Figs. 12 and 13 shall be

526   sliding rather than detachment. All the considered geometrical parameters of a bubble do not account

527   for the actual magnitude of forces. But they represent the qualitative implications of the associated

528   forces. Bubble size (R) and the bubble growth rates ($\dot{R}$) are repetitively used in models for both the

529   hindering and expediting forces for bubble departure. That is, some geometrical parameters have a

530   counteracting effect on bubble departure. As a consequence, estimating the bubble departure by a

531 single bubble geometrical parameter would not be sufficient. Hence, a proportional representation of

532 these geometrical parameters may provide a criterion for the bubble departure.

533

534 *4.2   Formulation of a bubble departure criterion*

535

536 The derivation of a bubble departure criterion based on geometrical parameters is not uncommon in

537 literature. Wu et al. [28] assumed that the effect of bubble contact angle is insignificant for bubble

538 departure and the surface tension force is proportional to the bubble base diameter. With this

539 assumption, they proposed a simple bubble departure criterion ($V_l \cdot R$= constant) that comprises the

540 bulk liquid velocity and the bubble size. Such an approach is improved further in the present work

541 with further considerations. As already discussed above, the buoyancy force (F_b) acts along the flow

542 direction and promotes bubble departure. R_{eq}^3 is the main factor in the expression of buoyancy force

543 (F_b). If the effect of bubble contact angle is neglected, then surface tension force (F_s) is mainly a

544 function of d_w. The surface tension force (F_s) impedes the departure of a bubble as it acts towards the

545 heater surface. One proportional term (d_w/R_{eq}^3) can be formulated out of these two forces. The

546 proposed term represents the dominating characteristics of the ratio of surface tension (F_s) and

547 buoyancy (F_b) forces. Apart from the buoyancy and surface tension force, three other forces

548 (F_{du}, $F_{growth,bulk}$ and F_{qs}) are considered as being influential for bubble departure. Among them, F_{du}

549 and $F_{growth,bulk}$ act in reverse directions and both of them are function of the bubble growth rate ($\dot{R}$).

550 The role of F_{qs} in the departure of a bubble is dependent on the (+ or -) sign of the relative velocity

551 ($\Delta V = V_l - V_b$). Considering the last three forces, another term as a function of bubble growth rate ($\dot{R}$)

552 and relative velocity ($V_l - V_b$) is suggested here. Hence, it is postulated that these terms decrease with

553 time and they become asymptotic when a bubble departs from its nucleation cavity. This means, that

554 unlike the bubble size, the importance of the bubble base diameter in the term (d_w/R_{eq}^3) reduces over

555 time. Another term was a function of $\dot{R}$ and ($V_l - V_b$). As both of these terms become asymptotic, their

556 time derivative is multiplied to find the minimum value. The relation then becomes as follows:

557

558
$$min\left\{ \frac{d}{dt}\left(\frac{d_w}{R_{eq}^3}\right) \cdot \frac{d}{dt}\left[f\left(\dot{R}, V_l - V_b\right)\right]\right\}. \tag{2 a}$$

559

560 This is proposed as a bubble departure criterion, i.e., a bubble departs from a nucleation cavity when

561 it satisfies Eqn. 2 a. The experimental data of the present study were used to propose a function

562     $f(\dot{R}\cdot(V_l\text{-}V_b))$. For that we considered the following options: $\dot{R}(V_l\text{-}V_b)$, $\dot{R}^2(V_l\text{-}V_b)$, $\dot{R}/(V_l\text{-}V_b)$ and

563     $\dot{R}^2/(V_l\text{-}V_b)$. The bubble diameters which agree with the proposed expression (Eqn. 2 a), have been

564   compared against the experimental results. From that is it found, that the numerically obtained

565   bubble diameters fit best against the experimental result for the following criterion:

566

567     $$min\left\{\frac{d}{dt}\left(\frac{d_w}{R_{eq}^3}\right)\cdot\frac{d}{dt}\left[\dot{R}_{eq}^2\left(V_l-V_b\right)\right]\right\}. \qquad\qquad\qquad (2\ b)$$

568

569   The comparison of the modelled and measured bubble departure diameters is shown in Fig. 14. The

570   experimentally measured bubble departure diameters for all the heater surfaces and bulk liquid

571   velocities for upward flow boiling are plotted along the x-axis of Fig. 14. The y-axis represents the

572   diameter of the bubbles obtained from Eqn. 2 b. 66% of the experimentally measured bubble

573   departure diameters satisfy the proposed criterion with ±10% deviation. 90% are within a ±25% of

574   error bound.

575

576   **5. Conclusion**

577

578   In the present study, we performed a thorough investigation on the influence of heater surface

579   characteristics and bulk liquid velocity on the departure dynamics of the isolated bubble during

580   nucleate boiling. We performed experiments using 9 different surfaces (θ_{hys} = 42.32° - 68.56°,

581   Sq = 0.01- 0.55 μm) for a range of bulk liquid velocity from 0.052 to 0.183 m/s and the heat fluxes of

582   39.41 to 45.47 kW/m². The experiments were conducted at atmospheric pressure with degassed-

583   deionized water at low-subcooling (1.9 ± 0.25 K) and the material of the test heaters was stainless

584   steel. High-resolution imaging technique was used to record the bubble life cycle. We may

585   summarize the experimental findings as follows:

586

587   i)   Bubble departure diameters decrease with the increase of bulk liquid velocity for all heater

588   surface characteristics. From averaged bubble departure diameters it was found that the decrease

589   of bubble departure diameter is greater for low bulk liquid velocity regime (0.052 - 0.16 m/s).

590

591   ii)   The bubble departure diameters were found to increase from 0.75 mm to 1.75 mm with the

592   increase of liquid contact angle hysteresis from 42.32° to 65.30°.

593

594 iii) The bubble growth rates were found largest for an intermediate roughness of Sq between 0.108
595   and 0.218 μm considering a range of bulk liquid velocity and heat flux. Larger bubble departure
596   diameters are obtained for surfaces with $Sq = 0.218$ μm.

597

598 iv) Finally, a bubble departure criterion was derived. 90% of the experimental bubble departure
599   diameters satisfy this criterion with ± 25% errors.

600

601 The outcome of this study may help to improve the numerical model to predict the bubble departure
602 diameter. The results provide further useful insights for designing the heat transfer surfaces.

603

604 **Acknowledgments**

605

610

611 **Conflict of interest**

612

613 There is no conflict of interests.

614

615 **References**

616

617 [1] S. Moghaddam, K. Kiger, Physical mechanisms of heat transfer during single bubble nucleate
618   boiling of FC-72 under saturation conditions-I. Experimental investigation. International
619   Journal of Heat and Mass Transfer, 2009. **52**: p. 1284-1294.
620 [2] R. Sugrue, J.B., T. McKrell, An experimental study of bubble departure diameter in
621   subcooled flow boiling including the effects of orientation angle, subcooling, mass flux, heat
622   flux and pressure. Nuclear Engineering and Design, 2014. **279**: p. 182-188.
623 [3] A. Zou, D. P. Singh, S. C. Maroo, Early evaporation of microlayer for boiling heat transfer
624   enhancement. Langmuir, 2016. **32**: p. 10808-10814.

625 [4] S. H. Kim, G. C. Lee, J. Y. Kang, K. Moriyama, H. S. Park, M. H. Kim, A study of nucleate
626   bubble growth on microstructured surface through high speed and infrared visualization.
627   International Journal of Multiphase Flow, 2017. **95**: p. 12-21.
628 [5] R. Sugrue, J. Buongiorno, A modified force-balance model for prediction of bubble departure
629   diameter in subcooled flow boiling. Nuclear Engineering and Design, 2016. **305**: p. 717-722.
630 [6] G. Sateesh, S. K. Das, A. R. Balakrishnan, Analysis of pool boiling heat transfer: effect of
631   bubbles sliding on the heating surface. International Journal of Heat and Mass Transfer, 2005.
632   **48**: p. 1543-1553.
633 [7] C. Gerardi, J. Buongiorno, L.W. Hu, T. McKrell, Study of bubble growth in water pool
634   boiling through synchronized, infrared thermometry and high-speed video. International
635   Journal of Heat and Mass Transfer, 2010. **53**: p. 4185-4192.
636 [8] M. A. Amidu, S. Jung, H. Kim, Direct experiment measurement for partitioning of wall heat
637   fluy during subcooled flow boiling: Effect of bubble areas of influence factor. International
638   Journal of Heat and Mass Transfer, 2018. **127**: p. 515-533.
639 [9] S.B. Jung, H.D. Kim, An experimental method to simultaneously measure the dynamics and
640   heat transfer associated with a single bubble during nucleate boiling on a horizontal surface.
641   International Journal of Heat and Mass Transfer, 2014. **73**: p. 365-375.
642 [10] W. Ding, E. Krepper, U. Hampel, Evaluation of the microlayer contribution to bubble growth
643   in horizontal pool boiling with a mechanistic model that considers dynamic contact angle and
644   base expansion. International Journal of Heat and Fluid Flow, 2018. **72**: p. 274-287.
645 [11] G. E. Thorncroft, J. F. Klausner, R. Mei, Bubble forces and detachment models. Multiphase
646   Science and Technology, 2001. **13**: p. 35-76.
647 [12] S. Raj, M. Pathak, M. K. Khan, An analytical model for predicting growth rate and departure
648   diameter of a bubble in subcooled flow boiling. International Journal of Heat and Mass
649   Transfer, 2017. **109**: p. 470-481.
650 [13] J. F. Klausner, R. Mei, D. M. Bernhard, L. Z. Zeng, Vapor bubble departure in forced
651   convection boiling. International Journal of Heat and Mass Transfer, 1993. **36**: p. 651-662.
652 [14] B. J. Yun, A. Splawski, S. Lo, C.H. Song, Prediction of a subcooled boiling flow with
653   advanced two-phase flow models. Nuclear Engineering Design, 2012. **253**: p. 351-359.
654 [15] Y.P. Chang, Some possible critical conditions in nuleate boiling. Journal of Heat Transfer,
655   1963. **85**: p. 89-100.
656 [16] Y.J. Cho, S.B. Yum, J.H. Lee, G.C.Park, Development of bubble departure and lift-off
657   diameter models in low heat flux and low flow velocity conditions. International Journal of
658   Heat and Mass Transfer, 2011. **54**: p. 3234-3244.

[17] H. T. Phan, N. Caney, P. Marty, S. Colasson, J. Gavillet, Surface wettability control by nanocoating: The effects on pool boiling heat transfer and nucleation mechanism. International Journal of Heat and Mass Transfer, 2009. **52**: p. 5459-5471.

[18] Y. Nam, J. Wu, G. Warrier, Y.S. Ju Experimental and numerical study of single bubble dynamics on a hydrophobic surface. Journal of Heat Transfer, 2009. **131**: p. 1-7.

[19] Y. Nam, E. Aktinol, V.K. Dhir, Y. S. Ju, Single bubble dynamics on a superhydrophilic surface with artificial nucleation sites. International Journal of Heat and Mass Transfer, 2011. **54**: p. 1572-1577.

[20] Y. L. Rousselet, Interacting effects of inertia and gravity on bubble dynamics, in Mechanical Engineering. 2014, University of California.

[21] Z. Sun, X. Chen,, H. Qiu, Bubble dynamics and heat transfer during pool boiling on wettability patterned surfaces. Heat Transfer Engineering, 2018. **39**: p. 663-671.

[22] D. Sarker, R. Franz, W. Ding, U. Hampel, Single bubble dynamics during subcooled nucleate boiling on a vertical heater surface: An experimental analysis of the effects of surface characteristics. International Journal of Heat and Mass Transfer, 2017. **109**: p. 907-921.

[23] P. Goel, A. K. Nayak, P. P. Kulkarni, J. B. Joshi, Experimental study on bubble departure characteristics in subcooled nucleate pool boiling. International Journal of Multiphase Flow, 2017. **89**: p. 163-176.

[24] D. Sarker, W. Ding, R. Franz, O. Varlamova, P. Kovats, K. Zähringer, U. Hampel, Investigations on the effects of heater surface characteristics on the bubble waiting period during nucleate boiling at low subcooling. Experimental Thermal and Fluid Science, 2019. **101**: p. 76-86.

[25] H.J. Jo, S.H. Kim, H. Kim, M. H. Kim, Nucleate boiling performance on nano/microstructures with different wetting surfaces. Nanoscale Research Letters, 2012. **7**.

[26] C.M. Kruse, T. Anderson, C. Wilson, C. Zuhlke, D. Alexander, G. Gogos, S. Ndao, Enhanced pool boiling heat transfer and critical heat flux on femtosecond laser processed stainless steel surfaces. International Journal of Heat and Mass Transfer, 2015. **82**: p. 109-116.

[27] D. Sarker, W. Ding, U. Hampel, Bubble growth during subcooled nucleate boiling on a vertical heater: A mechanistic attempt to evaluate the role of surface characteristics on microlayer evaporation. Applied Thermal Engineering, 2019. **153**: p. 565-574.

[28] W. Wu, P. Chen, B. G. Jones, T. A. Newell, A study on bubble detachment and the impact of heated surface structure in subcooled nucleate boiling flows. Nuclear Engineering and Design, 2008. **238**: p. 2693-2698.

693 [29] J. Yoo, C. E. Estrada-Perez, Y. A. Hassan, Experimental study of bubble dynamics and wall
694   heat transfer arising from a single nucleation site at subccoled flow boiling conidtions-Part 1:
695   Experimental methods and data quality verification. International Journal of Multiphase
696   Flow, 2016. **84**: p. 315-324.

697 [30] S. Maity, Effect of velocity and gravity on bubble dynamics, U.o. California, Editor. 2000.

698 [31] U. Harm, W. Fürbeth, K.-M. Mangold, K. Jüttner, Novel protective coatings for steel based
699   on a combination of self-assembled monolayers and conducting polymers, in
700   Macromolecular Symposia. 2002. p. 65-76.

701 [32] Y. Yuan, T. R. Lee, Contact angle and wetting properties [Chapter 1]. Surface Science
702   Techniques, 2013.

703 [33] C. Schneider, R. Hampel, A. Traichel, J. Herold, L. Kirsten, S. Meissner, E. Koch, A.
704   Hurtado. Experimental investigation of Nucleate boiling on optical transparent heated
705   surfaces with optical coherence tomograpgy (OCT) and infrared thermography. in 19th
706   International Conference on Nuclear Engineering. 2011. Chiba, Japan: JSME.

707 [34] W.H. McAdams, Heat transmission. 1942, New York: McGraw-Hill.

708 [35] J. C. Chen, Correlation for boiling heat transfer to saturated fluids in convective flow.
709   Industrial and Engineering Chemistry Process Design and Development, 1966. **5**: p. 322-329.

710 [36] S. Jung, H. Kim, Hydrdynamic formation of a microlayer underneath a boiling bubble.
711   International Journal of Heat and Mass Transfer, 2018. **120**: p. 1229-1240.

712
713
714
715
716
717
718
719
720
721
722
723
724
725
726

727 **Figures:**
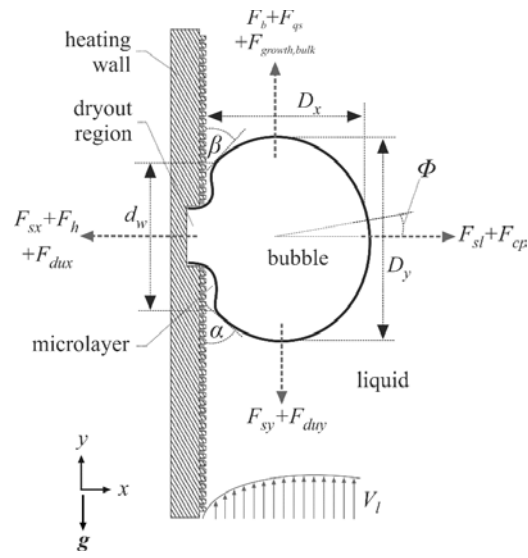
728

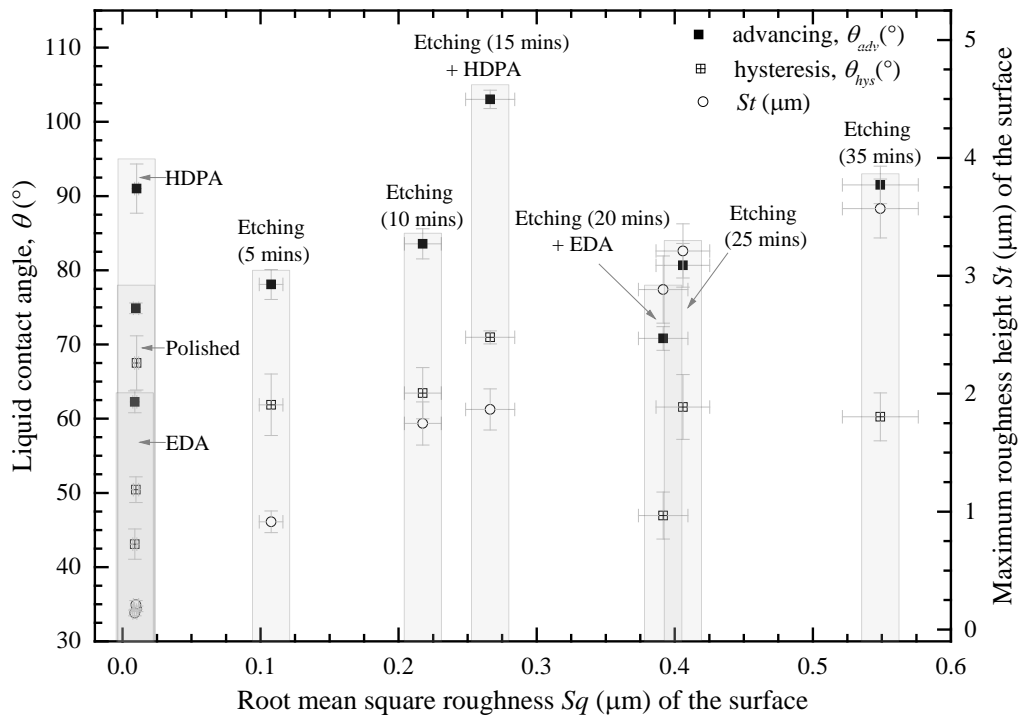729 *Fig. 1: Forces acting on the bubble during upward flow boiling.*

730

731

732

733

734

735

736

737

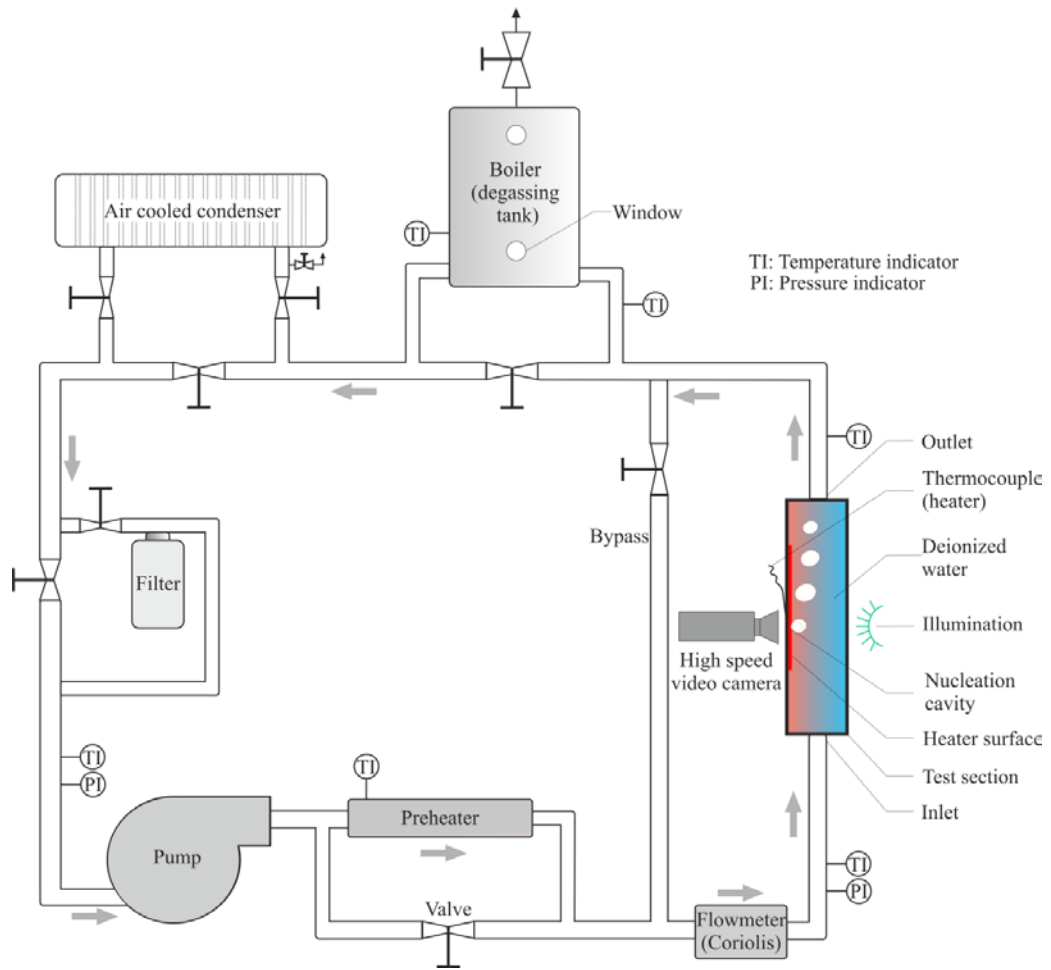*Fig. 2: Surface parameters and the corresponding preparation methods of the test samples.*

738

739

740

741
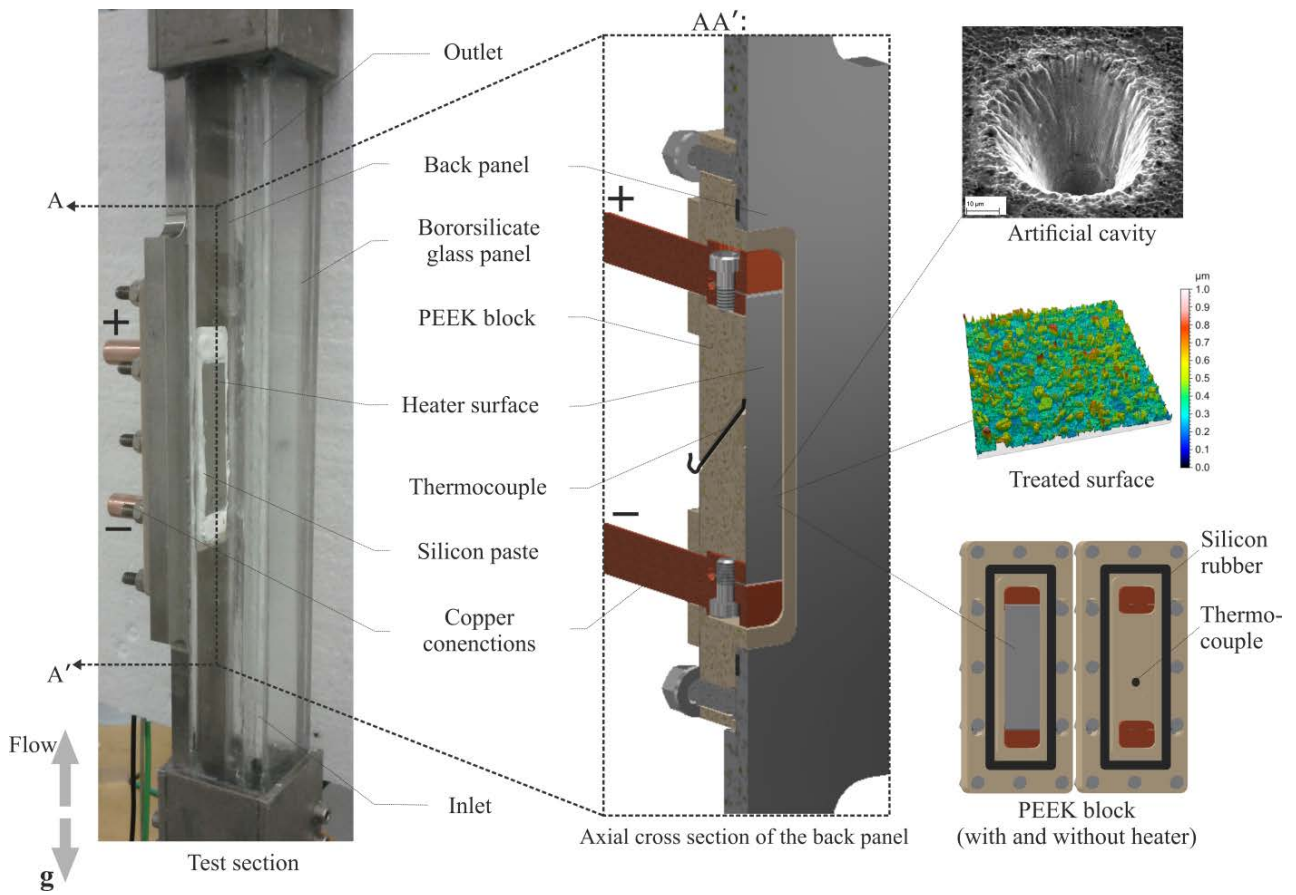
Fig. 3. A schematic of the experimental facility.

743

744

Outlet

Back panel

Bororsilicate glass panel

PEEK block

Heater surface

Thermocouple

Silicon paste

Copper conenctions

Inlet

Flow

g

Test section

AA':

Axial cross section of the back panel

Artificial cavity

Treated surface

Silicon rubber

Thermocouple

PEEK block (with and without heater)

Fig. 4. Details of the test section.

745
746
747
748
749
750
751
752
753
754
755
756
757
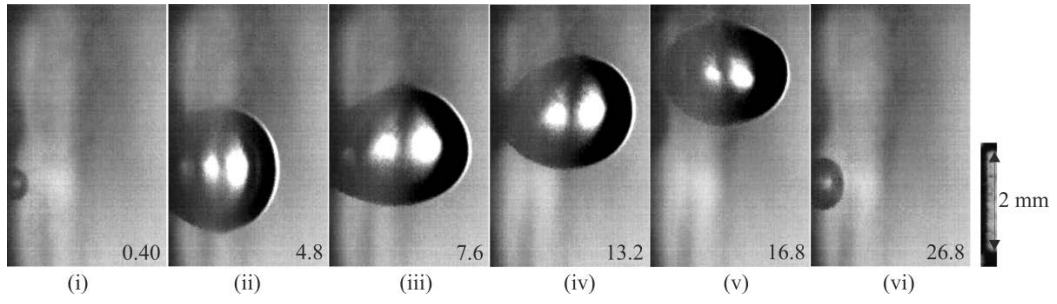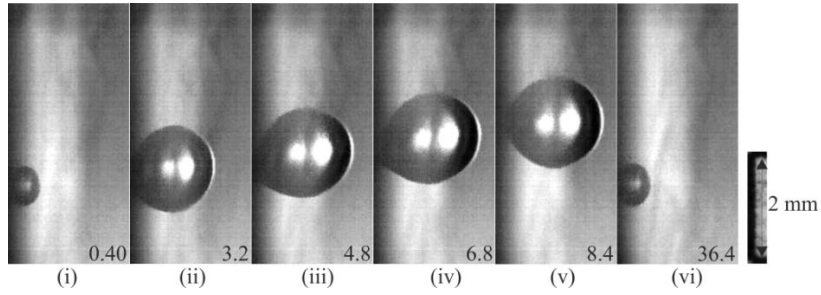
Fig. 5. Video sequence showing the different stages of a bubble ebullition cycle on $Sq = 0.01$ μm, $\theta_{hys} = 65.3°$ for $q'' = 42.44$ kW/m², $\Delta T_w = 9.20$ K, $\Delta T_{sub} = 2.10$ K, 0.052 m/s (a), $q'' = 42.44$ kW/m², $\Delta T_w = 6.56$ K, $\Delta T_{sub} = 1.72$ K, 0.183 m/s (b).
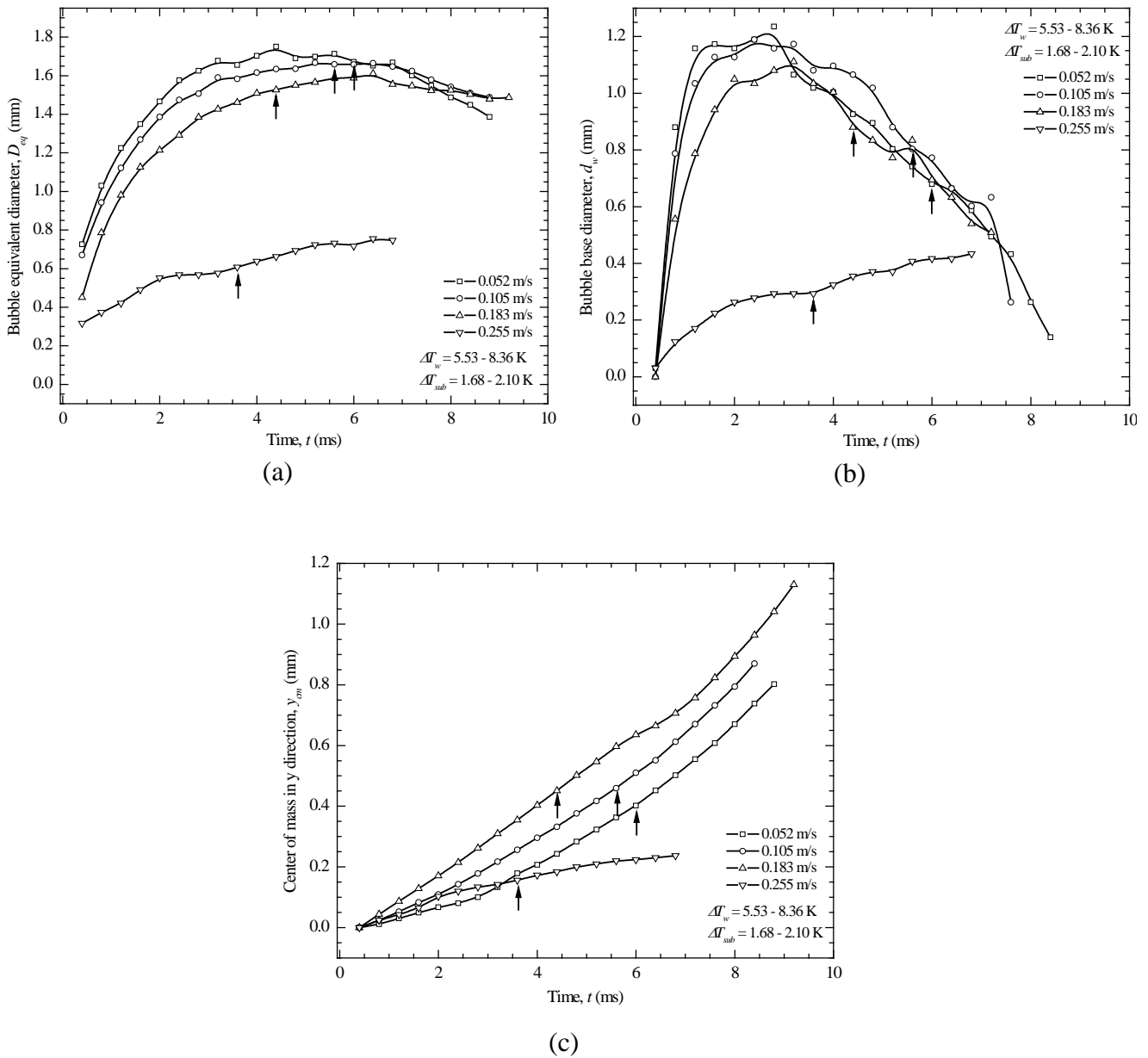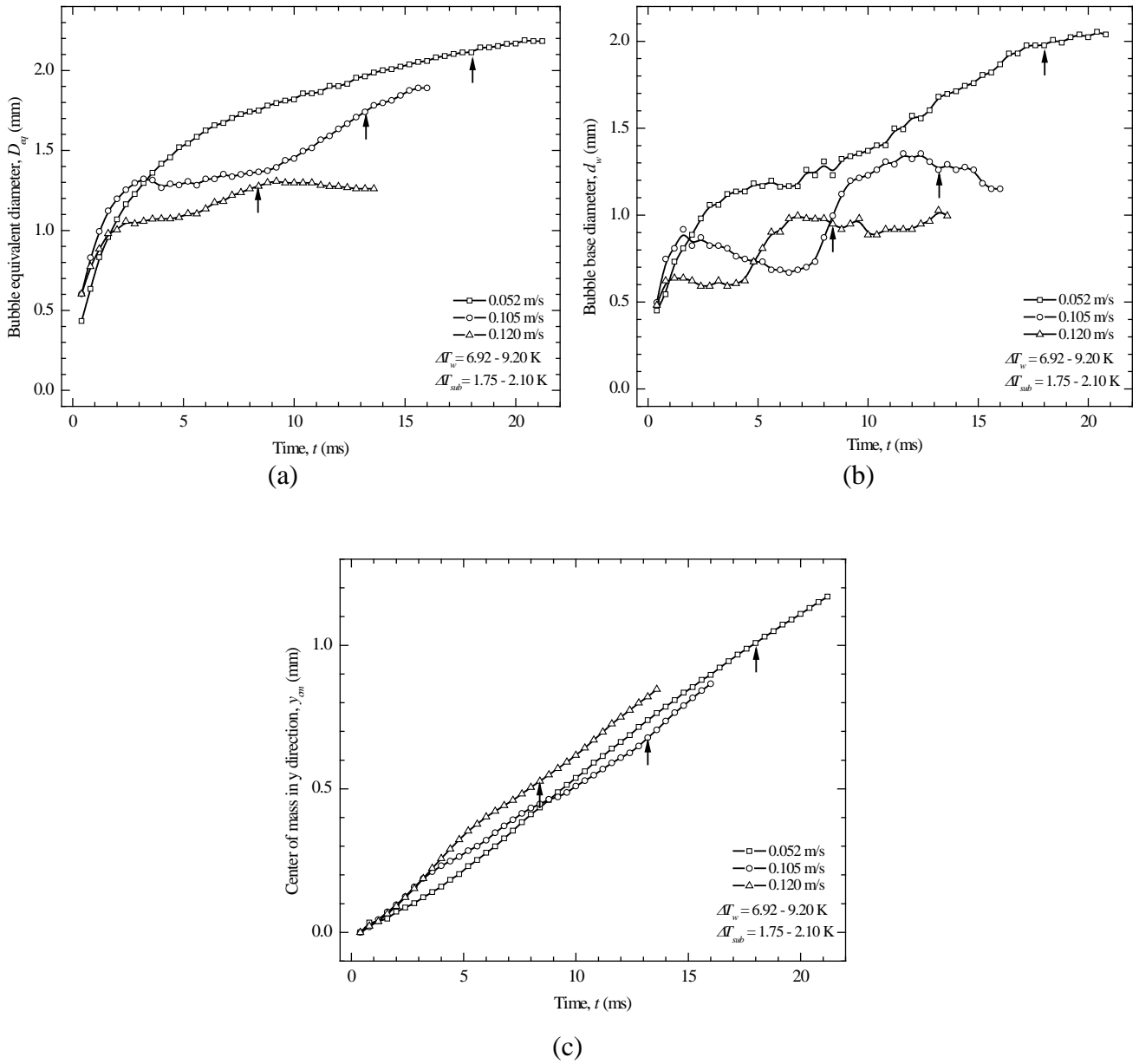
(a)

(b)

(c)

Fig. 6. Bulk liquid velocity effect on the temporal evolution of the bubble equivalent diameter (a), bubble base diameter (b) and center of mass of bubble (c) for Sq = 0.01 μm, θ$_{hys}$ = 65.30° and q″ = 39.41 kW/m². ↑ indicates the bubble departure point.

772

Fig. 7. Bulk liquid velocity effect on the temporal evolution of the bubble equivalent diameter (a), bubble base diameter (b) and center of mass of bubble (c) for Sq = 0.218 μm, θ$_{hys}$ = 61.47° and q″ = 42.44 kW/m². ↑ *indicates the bubble departure point.*
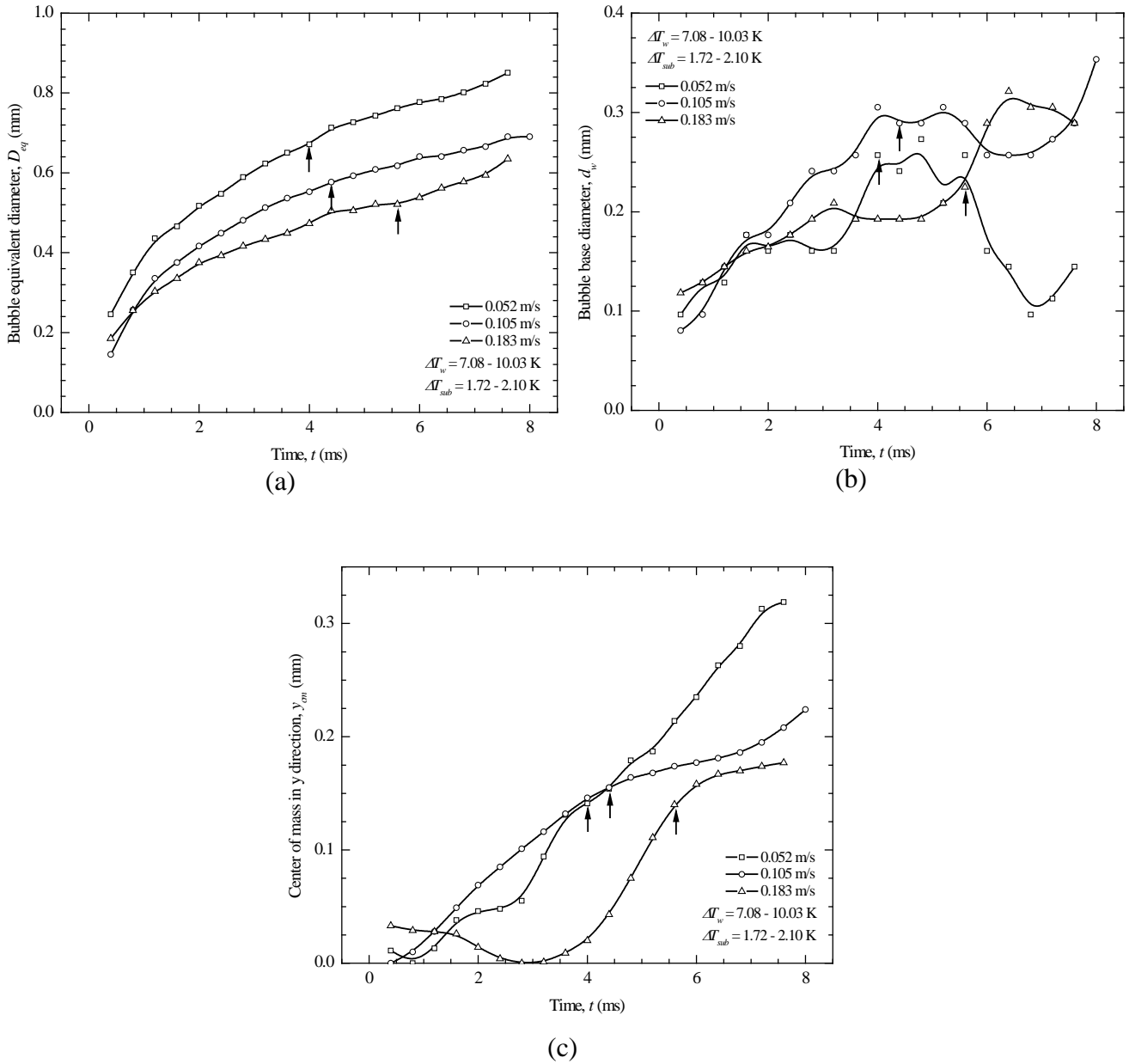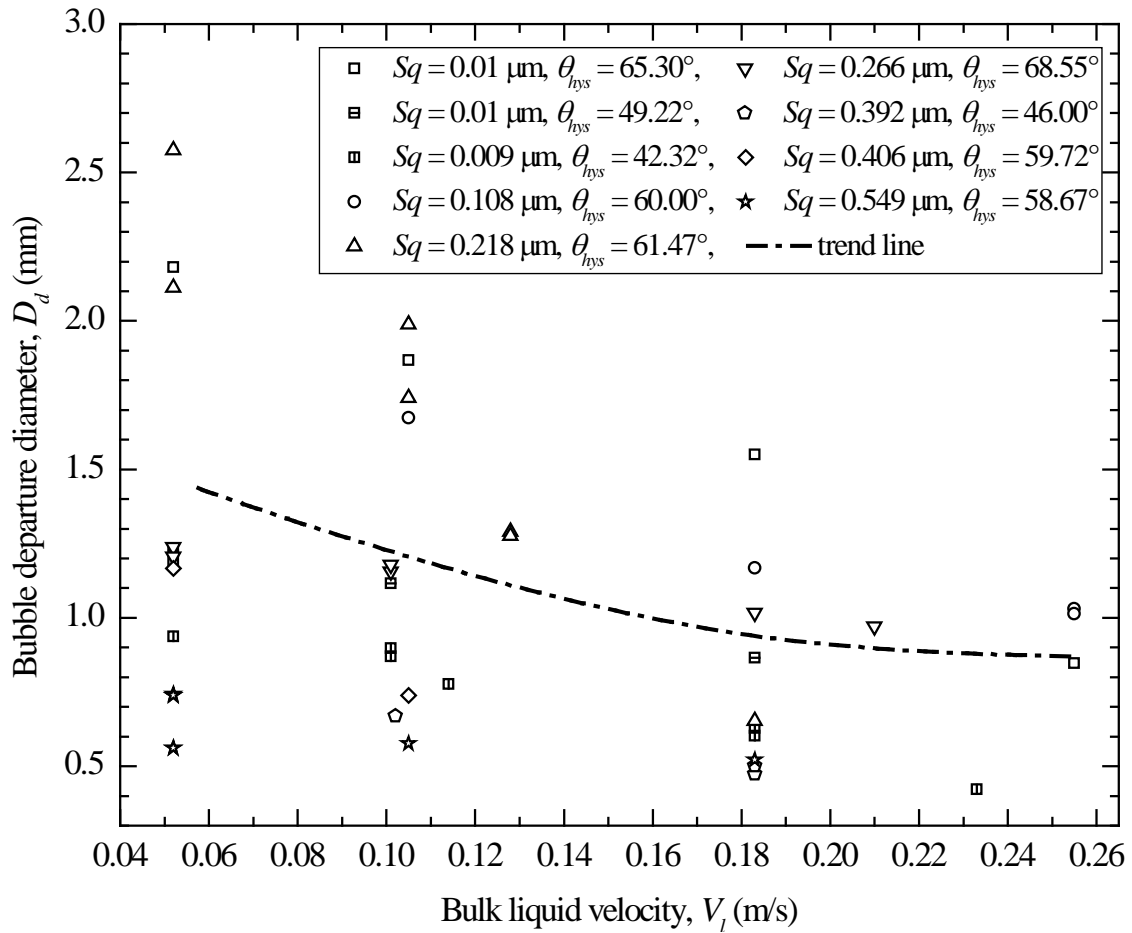
773

30

Fig. 8. Bulk liquid velocity effect on the temporal evolution of the bubble equivalent diameter (a), bubble base diameter (b) and center of mass of bubble (c) for $Sq = 0.549 \mu m$, $\theta_{hys} = 58.47°$ and $q'' = 45.47 kW/m^2$. ↑ indicates the bubble departure point.

774

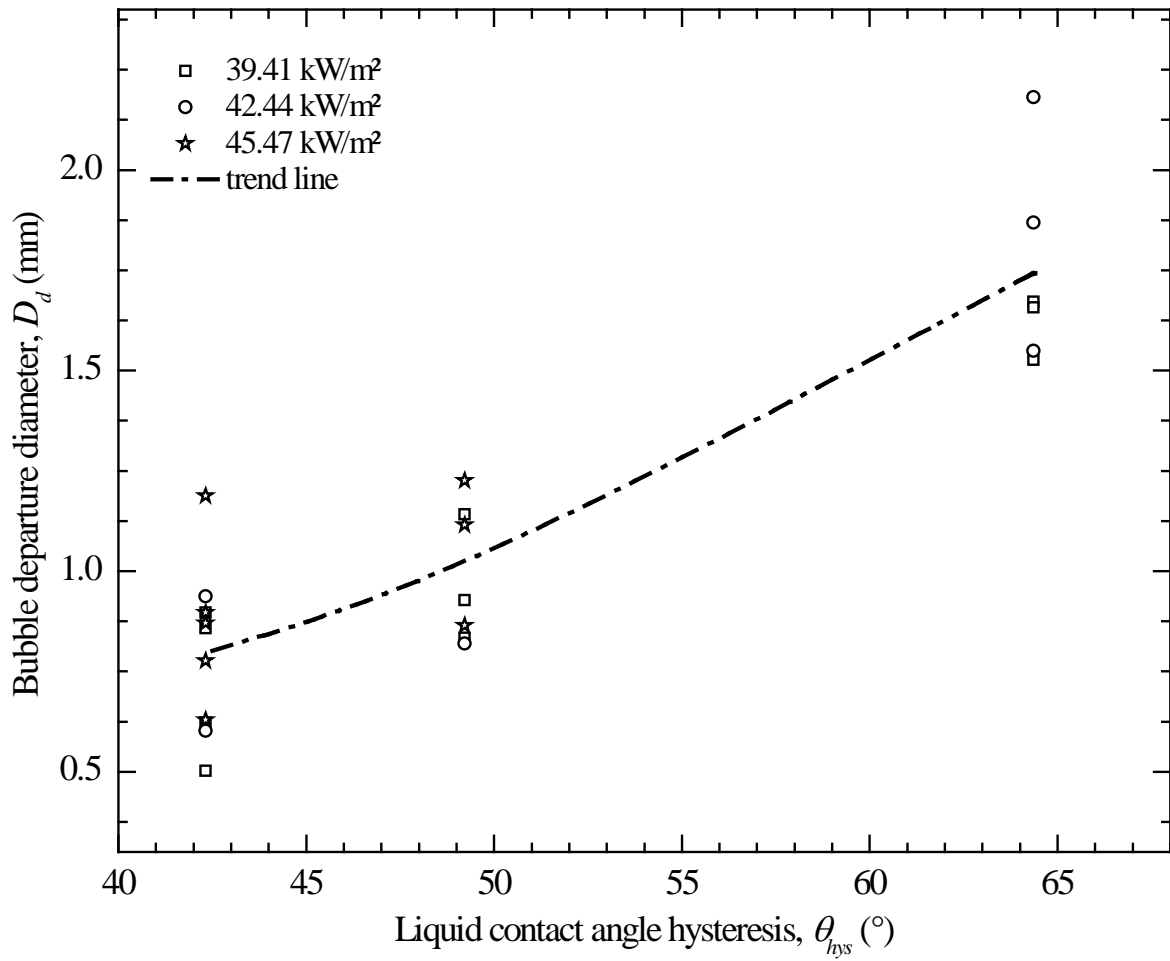Fig. 9. Effect of bulk liquid velocity on the bubble departure ($q'' = 42.44 - 45.47$ kW/m², $\Delta T_w = 6.03 - 10.03$ K, $\Delta T_{sub} = 1.90 \pm 0.20$ K).

785

Fig. 10. Effect of heater surface wettability on the bubble departure (ΔT_w = 6.03 - 10.03 K,
ΔT_{sub} = 1.90 ± 0.20 K, V_l = 0.052 - 0.183 m/s).*

788

789

790

791

792

793

794

795
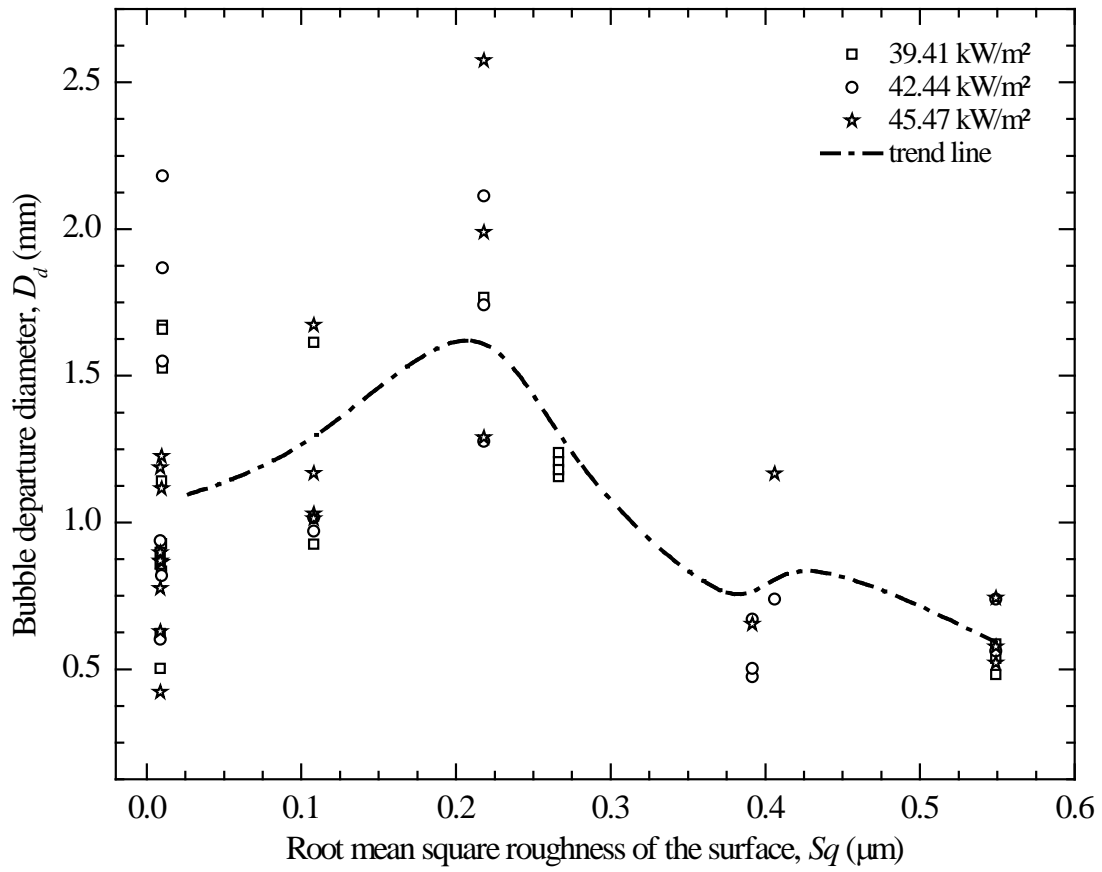
796

797 *Fig. 11. Effect of heater surface roughness on bubble departure diameter ($\Delta T_w = 6.03$ - 10.03 K,*

798 $\Delta T_{sub} = 1.90 \pm 0.20$ K, $V_l = 0.052$ - 0.183 m/s).

799

800

801
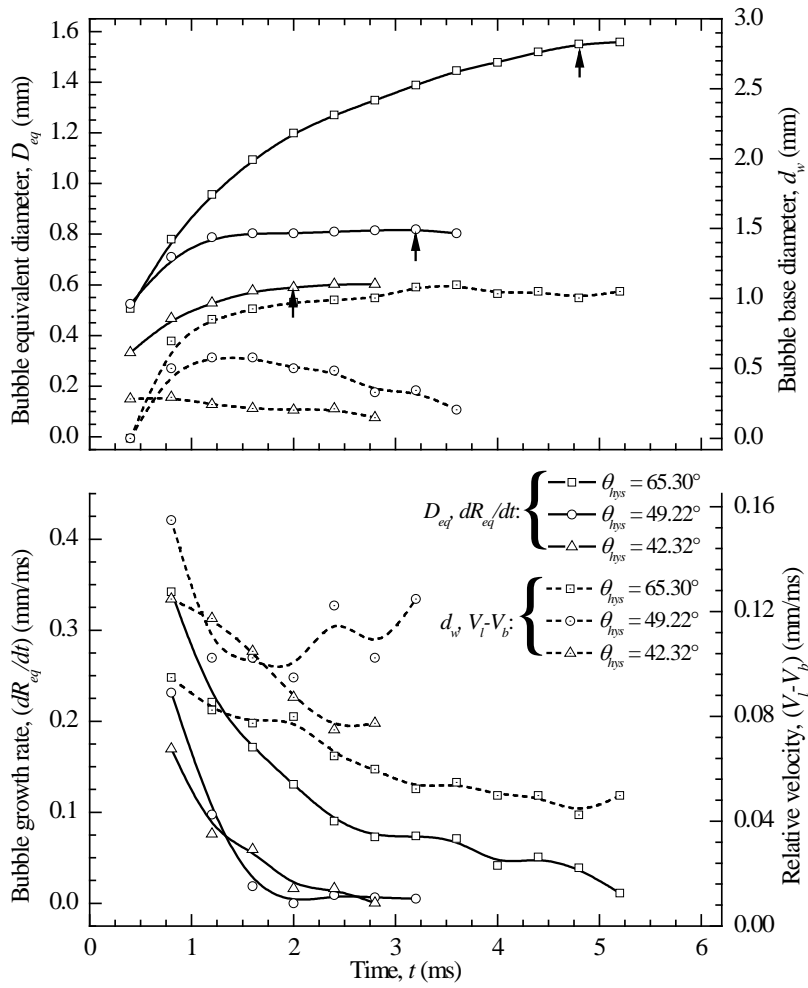
Fig. 12. Effect of influential parameters on the bubble departure for surfaces with different wetting characteristics (q″ = 42.44 kW/m², ΔT_w = 6.56 K, ΔT_sub = 1.72 K, V_l = 0.183 m/s). ↑ indicates the bubble departure point.

805

806

807
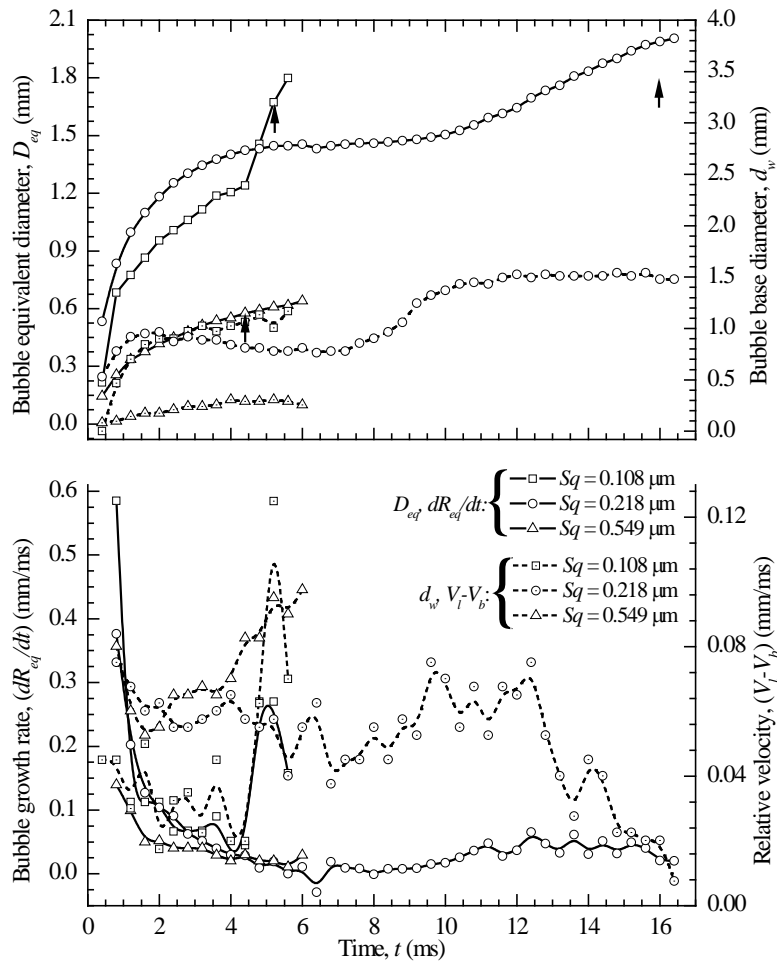
Fig. 13. Effect of influential parameters on the bubble departure for surfaces with different roughness ($q'' = 45.47$ kW/m², $\Delta T_w = 8.70$ K, $\Delta T_{sub} = 1.76$ K, $V_l = 0.105$ m/s). ↑ indicates the bubble departure point.

808
809
810

811

812
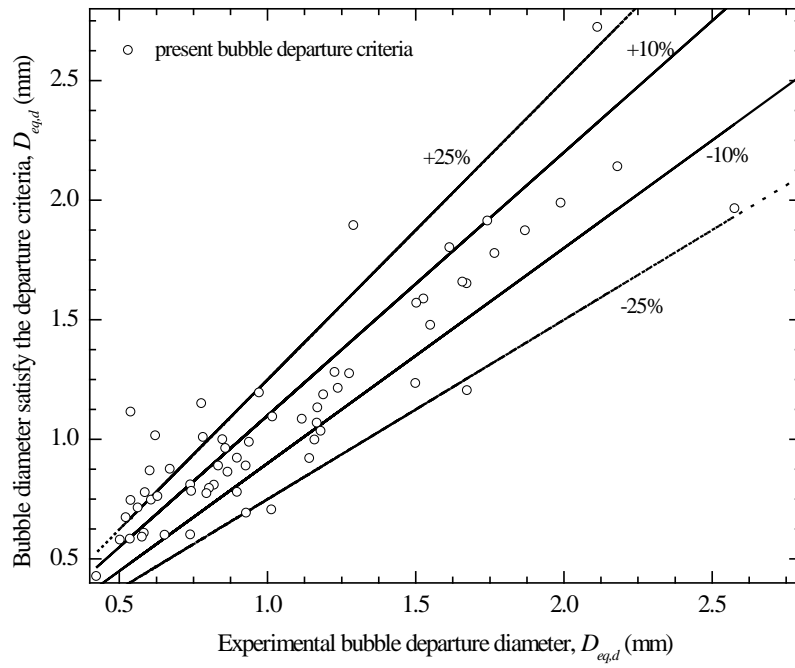
Fig. 14. Comparison of experimental and numerical bubble departure diameter.

Tables:

Table 1: Measurement and calculation uncertainties.

Parameters	Instruments	Locations	Uncertainties		Total uncertainties
			Calibration/static	Measurement	
Temperature	K-type thermocouples	Test section inlet	± 0.50 K	± 0.30 K	± 0.58 K
		Test section outlet	± 0.50 K	± 0.20 K	± 0.54 K
		Heater wall	± 0.30 K	± 0.63 K	± 0.70 K
Flow meter	Coriolis mass flow meter	Test section inlet	± 0.20%	± 1.70%	± 1.71%
Heat flux	Power supply, DAS	Heater wall	± 5.02%	± 5.04%	± 7.12%
Bubble sizes	HSVC				± 40.985 μm

Table 2: Simplified expressions for the forces governing bubble departure [5, 11].

Force	Expression	Simplification
Surface tension force	$F_{sy} = -1.25 d_w \sigma \dfrac{\pi(\alpha-\beta)}{\pi^2 - (\alpha-\beta)^2}(sin\,\alpha + sin\,\beta).$ $F_{sy} = -d_w \sigma \dfrac{\pi}{(\alpha-\beta)}(cos\,\beta - cos\,\alpha).$	$F_s = f(d_w, \alpha, \beta).$
Buoyancy force	$F_b = \dfrac{4}{3}\pi R^3 (\rho_l - \rho_g) g.$	$F_b = f(R).$
Unsteady drag force	$F_{duy} = -\rho_l \pi R^2 \left(\dfrac{3}{2}C_s \dot{R}^2 - R\ddot{R}^2\right) sin\,\varphi.$ $F_{dux} = -\rho_l \pi R^2 \left(\dfrac{3}{2}C_s \dot{R}^2 - R\ddot{R}^2\right) cos\,\varphi.$	$F_{du} = f(R, \dot{R}, \varphi).$
Quasi-steady drag force	$F_{qs} = 6\pi \nu \rho_l \Delta V R \left[\dfrac{2}{3} + \left[\left(\dfrac{12}{Re_b}\right)^{0.65} + 0.796^{0.65}\right]^{-1/0.65}\right].$	$F_{qs} = f(\Delta V, R).$
Additional added-mass	$F_{growth,bulk} = 2\pi \rho_l R^2 V_{lx} \dot{R}.$	$F_{growth,bulk} = f(R, \dot{R}, V_l).$
Contact pressure force	$F_{cp} = \dfrac{\pi d_w^2}{4}\dfrac{2\sigma}{5R}.$	$F_{cp} = f(d_w, R).$
Shear lift force	$F_{sl} = \dfrac{1}{2}\rho_l \Delta V^2 \pi R^2 \left[3.877 G_s^{0.5}\left[Re_b^{-2} + 0.014 G_s^2\right]^{0.25}\right].$ $C_L = 0.8 G_s$, $G_s = \dfrac{dV}{dx}\dfrac{R}{\Delta V}.$	$F_{sl} = f(\Delta V, R).$
Hydrodynamic pressure force	$F_h = \dfrac{9}{8}\rho_l \Delta V^2 \dfrac{\pi d_w^2}{4}.$	$F_h = f(\Delta V, d_w).$

Appendix

864
<div align="center">Table 3: Experimental parameters.</div>

Surface parameters				Heat flux q'' (kW/m²)	Bulk liquid velocity V_l (m/s)	Subcooling ΔT_{sub} (K)	Wall superheat ΔT_w (K)
Roughness	Wettability						
Rms roughness Sq (µm)	Advancing θ_{adv} (°)	Receding θ_{rec} (°)	Hysteresis θ_{hys} (°)				
0.01023	91	25.7	65.3	39.41	0.052	2.1	8.36
0.01023	91	25.7	65.3	39.41	0.105	1.76	7.14
0.01023	91	25.7	65.3	39.41	0.183	1.72	6.03
0.01023	91	25.7	65.3	39.41	0.255	1.68	5.53
0.01023	91	25.7	65.3	42.44	0.052	2.1	9.196
0.01023	91	25.7	65.3	42.44	0.105	1.76	7.924
0.01023	91	25.7	65.3	42.44	0.183	1.72	6.56
0.01023	91	25.7	65.3	42.44	0.255	1.68	6.24
0.00976	74.87	25.65	49.22	39.41	0.052	2.1	8.36
0.00976	74.87	25.65	49.22	39.41	0.105	1.76	7.14
0.00976	74.87	25.65	49.22	39.41	0.183	1.72	6.03
0.00976	74.87	25.65	49.22	42.44	0.183	1.72	6.56
0.00976	74.87	25.65	49.22	45.47	0.052	2.1	10.032
0.00976	74.87	25.65	49.22	45.47	0.105	1.76	8.698
0.00976	74.87	25.65	49.22	45.47	0.183	1.72	7.08
0.0089	62.27	19.95	42.32	39.41	0.052	2.1	8.36
0.0089	62.27	19.95	42.32	39.41	0.105	1.76	7.14
0.0089	62.27	19.95	42.32	39.41	0.183	1.72	6.03
0.0089	62.27	19.95	42.32	42.44	0.052	2.1	9.196
0.0089	62.27	19.95	42.32	42.44	0.183	1.72	6.56
0.0089	62.27	19.95	42.32	45.47	0.052	2.1	10.032
0.0089	62.27	19.95	42.32	45.47	0.101	1.76	8.698
0.0089	62.27	19.95	42.32	45.47	0.115	1.74	8.1
0.0089	62.27	19.95	42.32	45.47	0.184	1.72	7.08
0.0089	62.27	19.95	42.32	45.47	0.233	1.7	6.5
0.2663	104.02	35.47	68.55	39.41	0.052	2.1	8.36
0.2663	104.02	35.47	68.55	39.41	0.101	1.76	7.14
0.3915	70.814	24.864	45.95	42.44	0.103	1.76	7.924
0.3915	70.814	24.864	45.95	42.44	0.183	1.72	6.56
0.3915	70.814	24.864	45.95	45.47	0.183	1.72	7.08
0.108	78.08	18.09	59.99	39.41	0.052	2.1	8.36
0.108	78.08	18.09	59.99	39.41	0.183	1.72	6.03

0.108	78.08	18.09	59.99	42.44	0.183	1.72	6.56
0.108	78.08	18.09	59.99	42.44	0.210	1.7	6.06
0.108	78.08	18.09	59.99	45.47	0.105	1.76	8.698
0.108	78.08	18.09	59.99	45.47	0.183	1.72	7.08
0.108	78.08	18.09	59.99	45.47	0.256	1.68	7.01
0.218	83.55	22.08	61.47	39.41	0.052	2.1	8.36
0.218	83.55	22.08	61.47	42.44	0.052	2.1	9.196
0.218	83.55	22.08	61.47	42.44	0.105	1.76	7.924
0.218	83.55	22.08	61.47	42.44	0.120	1.75	6.924
0.218	83.55	22.08	61.47	45.47	0.052	2.1	10.032
0.218	83.55	22.08	61.47	45.47	0.105	1.76	8.698
0.218	83.55	22.08	61.47	45.47	0.128	1.75	7.28
0.406	78.66	18.94	59.72	42.44	0.105	1.76	7.924
0.406	78.66	18.94	59.72	45.47	0.052	2.1	10.032
0.549	91.49	32.82	58.67	39.41	0.052	2.1	8.36
0.549	91.49	32.82	58.67	39.41	0.105	1.76	7.14
0.549	91.49	32.82	58.67	42.44	0.052	2.1	9.196
0.549	91.49	32.82	58.67	42.44	0.105	1.76	7.924
0.549	91.49	32.82	58.67	45.47	0.052	2.1	10.032
0.549	91.49	32.82	58.67	45.47	0.105	1.76	8.698
0.549	91.49	32.82	58.67	45.47	0.183	1.72	7.08

865